Computer Modeling in Engineering & Sciences

Tech Science Press

DOI: 10.32604/cmes.2024.046770

ARTICLE

The Boundary Element Method for Ordinary State-Based Peridynamics

Xue Liang[1,2] **and Linjuan Wang**[3,*]

[1]State Key Laboratory for Turbulence and Complex Systems, Department of Mechanics and Engineering Science, College of Engineering, Peking University, Beijing, 100871, China

[2]CAPT-HEDPS, and IFSA Collaborative Innovation Center of MoE, College of Engineering, Peking University, Beijing, 100871, China

[3]School of Astronautics, Beihang University, Beijing, 100191, China

*Corresponding Author: Linjuan Wang. Email: wanglj@buaa.edu.cn

Received: 14 October 2023 Accepted: 26 December 2023 Published: 11 March 2024

ABSTRACT

The peridynamics (PD), as a promising nonlocal continuum mechanics theory, shines in solving discontinuous problems. Up to now, various numerical methods, such as the peridynamic mesh-free particle method (PD-MPM), peridynamic finite element method (PD-FEM), and peridynamic boundary element method (PD-BEM), have been proposed. PD-BEM, in particular, outperforms other methods by eliminating spurious boundary softening, efficiently handling infinite problems, and ensuring high computational accuracy. However, the existing PD-BEM is constructed exclusively for bond-based peridynamics (BBPD) with fixed Poisson's ratio, limiting its applicability to crack propagation problems and scenarios involving infinite or semi-infinite problems. In this paper, we address these limitations by introducing the boundary element method (BEM) for ordinary state-based peridynamics (OSPD-BEM). Additionally, we present a crack propagation model embedded within the framework of OSPD-BEM to simulate crack propagations. To validate the effectiveness of OSPD-BEM, we conduct four numerical examples: deformation under uniaxial loading, crack initiation in a double-notched specimen, wedge-splitting test, and three-point bending test. The results demonstrate the accuracy and efficiency of OSPD-BEM, highlighting its capability to successfully eliminate spurious boundary softening phenomena under varying Poisson's ratios. Moreover, OSPD-BEM significantly reduces computational time and exhibits greater consistency with experimental results compared to PD-MPM.

KEYWORDS

Ordinary state-based peridynamics; boundary element method; crack propagation; fracture toughness

1 Introduction

Peridynamics, as a nonlocal continuum mechanics theory, has garnered increasing attention owing to its notable advantage in addressing discontinuous problems [1,2]. This advantage arises from its unique approach of replacing spatial differential operators with integral operators in the equilibrium equation. Over time, peridynamic theory has seen continuous development and improvement, leading to the introduction of various theoretical models, e.g., the dual horizon peridynamics

[3,4], nonlocal operator methods [5], element-based peridynamic models [6,7], viscoelastic models [8], and elastoplastic theories [9]. At the same time, a series of numerical approaches have emerged to leverage the advantages of Peridynamics (PD) in addressing various issues, including discontinuous problems [10,11], microscale problems [12,13] and multiscale problems [14–16]. The one gaining the most attention is the Peridynamic Mesh-free Particle Method (PD-MPM), where the peridynamic equilibrium equation is discretized directly in terms of timing and spacing [17]. Kilic et al. [18] explored a collocation point method drawing support from the Gaussian integral formula to optimize the nonlocal numerical integrals in the PD-MPM. Chen et al. [19] proposed the peridynamic finite element method (PD-FEM), drawing support from the energy principle. Tian et al. [20] adopted a central difference scheme for handling the PD equation. Liang et al. [21] put forward the bond-based peridynamics (BBPD) boundary element method (BBPD-BEM).

Several coupled numerical methods have been proposed based on the fundamental numerical approaches mentioned above. For example, to enhance computational efficiency, PD-MPM is coupled with numerical methods of classical continuum mechanics [22–26]. These coupled methods essentially integrate two types of continuum mechanical media: the PD medium and the classical continuum medium. However, utilizing these coupled methods for investigating the responses of a single-phase material may result in a mismatch between numerical models and the actual research project. To address this issue, it is more advisable to couple different peridynamic numerical methods, such as PD-MPM with PD-FEM or PD-BEM. Therefore, the advancement of fundamental methods, including PD-MPM, PD-FEM, and PD-BEM, holds crucial importance for the practical applications of peridynamics. It is worth clarifying the term "PD-BEM" to avoid misunderstandings. PD-BEM is a numerical method constructed based on peridynamic theory, differing from numerical methods that combine the classical local continuum theory's Boundary Element Method (BEM) with the mesh-free particle method based on peridynamic theory [25–28].

Our research is dedicated to PD-BEM, a focal point that offers distinct advantages. In comparison to alternative numerical methods, BEM stands out for its efficiency enhancement achieved through dimension reduction [21]. Specifically, BBPD-BEM exhibits computational speeds two orders of magnitude faster than PD-MPM in computational domains without destruction. Furthermore, BBPD-BEM effectively circumvents spurious boundary-softening phenomena, facilitating PD calculations in infinite domains. However, it is essential to acknowledge that BBPD-BEM is built upon BBPD, which features only one independent material parameter for isotropic peridynamic materials. Additionally, the absence of a crack propagation model in BBPD-BEM restricts its ability to address crack propagation problems. To overcome these limitations, our paper aims to introduce BEM for ordinary state-based peridynamics (OSPD), one of the two typologies of state-based PD [2]. Within the numerical framework of OSPD-BEM, we propose the crack propagation model inspired by the cohesive crack model [29–31] and the PD bilinear model [32,33]. This approach addresses the identified shortcomings in BBPD-BEM, enhancing its versatility and applicability.

The process of outlining the BEM for OSPD, referred to as OSPD-BEM, unfolds through the following steps. Firstly, a boundary integral equation (BIE) for OSPD is derived, drawing support from Green's function [34,35] and the nonlocal operator theory [36,37] in Section 2. Following this, a crack propagation model for the OSPD-BEM is proposed in Section 3. In Section 4, the accuracy and efficiency of OSPD-BEM are then demonstrated through the presentation of four numerical examples. The conclusions are given in Section 5. For ease of reading, the symbols in the paper are listed in Table 1 before the text begins.

Table 1: Nomenclature

Mark	Explanation	Mark	Explanation
Ω_{τ_d}	Displacement volume-constrained boundary	Ω_τ	Volume-constrained boundary
$\partial\Omega_d$	Local displacement boundary	ν	Theoretical Poisson's ratio
Ω_{τ_n}	Force volume-constrained boundary	$\tilde{\nu}$	Numerical Poisson's ratio
$\mathscr{B}_\Gamma^*$	Adjoint operator of weighted nonlocal divergence	Ω	Solution domain
$\tilde{\mathbf{u}}_g$	Green's function in Laplace domain	ρ	Mass density
$\mathscr{G}$	Peridynamic Navier equilibrium operator	$\mathbf{n}$	Unit normal vector
$\mathscr{B}$	Nonlocal divergence operator	$\partial\Omega_n$	Local force boundary
$\overline{\mathbf{T}}$	Peridynamic force flux vector operator	$\mathscr{M}$	Nonlocal interaction operator
$\mathscr{B}^*$	Adjoint operator of nonlocal divergence	$\mathrm{h_r}$	Horizon
$\mathscr{M}$	Peridynamic Navier flux operator	$\Xi(\mathbf{x})$	Dirac function
$\mathbf{u}_G$	Infinite domain Green's function	$\partial\Omega$	Local boundary

2 The Boundary Integral Equation

Firstly, we briefly introduce the linear elastic OSPD [38,39] with the volume-constrained boundary [40,41]. The equilibrium equation for the linear elastic OSPD is as follows [37]:

$$\begin{cases} \mathscr{B}\left(\boldsymbol{\varphi}\boldsymbol{\varpi}\left(\mathscr{B}^*(\mathbf{u})\right)^{\mathrm{T}} + \Gamma\chi\mathscr{T}_{\mathrm{r}}\left(\mathscr{B}_\Gamma^*(\mathbf{u})\right)\mathbf{I}\right)(\mathbf{x}) + \mathbf{F}_{\mathrm{b}}(\mathbf{x}) = \mathbf{0} & \text{for } \mathbf{x}\in\Omega \\ \mathbf{u}(\mathbf{x}) = \mathbf{h}_{\mathrm{u}}(\mathbf{x}) & \text{for } \mathbf{x}\in\Omega_{\tau_d} \\ \mathscr{M}\left(\boldsymbol{\varphi}\boldsymbol{\varpi}\left(\mathscr{B}^*(\mathbf{u})\right)^{\mathrm{T}} + \Gamma\chi\mathscr{T}_{\mathrm{r}}\left(\mathscr{B}_\Gamma^*(\mathbf{u})\right)\mathbf{I}\right)(\mathbf{x}) = \mathbf{g}_\sigma(\mathbf{x}) & \text{for } \mathbf{x}\in\Omega_{\tau_n} \end{cases} \tag{1}$$

where φ and χ are the material parameters; ϖ and Γ are the nonlocal weighting functions [42]; $\mathbf{u}(\mathbf{x})$ is displacement vector; the superscript T is transposed symbol; $\mathscr{T}_{\mathrm{r}}$ denotes trace operator; $\mathbf{I}$ is metric tensor; $\mathbf{x}$ is location vector corresponding to single material point; $\mathbf{F}_{\mathrm{b}}(\mathbf{x})$ denotes body force density; $\mathbf{h}_{\mathrm{u}}(\mathbf{x})$ denotes a given displacement constraint on displacement boundary Ω_{τ_d}; $\mathbf{g}_\sigma(\mathbf{x})$ denotes a given force boundary condition on force boundary Ω_{τ_n}. Ω_{τ_d} and Ω_{τ_n} are a portion of volume-constrained boundary Ω_τ that is a banded area surrounding the classical local boundary $\partial\Omega$. They satisfy $\Omega_\tau = \Omega_{\tau_n}\cup\Omega_{\tau_d}$. An explicit explanation can be acquired in the literature [21,36]. Ω, Ω_τ, Ω_{τ_d}, Ω_{τ_n} and $\partial\Omega$ are schematically explained in Fig. 1. Incidentally, $\partial\Omega_d$ is the classical local displacement boundary; $\partial\Omega_n$ is the classical local force boundary. The nonlocal operators $\mathscr{B}$, $\mathscr{B}^*$, $\mathscr{B}_\Gamma^*$ and $\mathscr{M}$ in Eq. (1) are defined as [36]

$$\mathscr{B}(\mathbf{Q})(\mathbf{x}) \equiv \int_{\Omega\cup\Omega_\tau} [\mathbf{Q}(\mathbf{x},\mathbf{y}) + \mathbf{Q}(\mathbf{y},\mathbf{x})]\cdot\boldsymbol{\beta}(\mathbf{x},\mathbf{y})\,\mathrm{d}V_{\mathrm{y}} \qquad \text{for } \mathbf{x}\in\Omega \tag{2}$$

$$\mathscr{B}^*(\mathbf{P})(\mathbf{x},\mathbf{y}) \equiv -[\mathbf{P}(\mathbf{y}) - \mathbf{P}(\mathbf{x})]\otimes\boldsymbol{\beta}(\mathbf{x},\mathbf{y}) \qquad \text{for } \mathbf{x},\mathbf{y}\in\Omega\cup\Omega_\tau \tag{3}$$

$$\mathscr{B}_\Gamma^*(\mathbf{x}) \equiv \int_{\Omega\cup\Omega_\tau} \mathscr{B}^*(\mathbf{Q})(\mathbf{x},\mathbf{y})\,\Gamma(\mathbf{x},\mathbf{y})\,\mathrm{d}V_{\mathrm{y}} \qquad \text{for } \mathbf{x}\in\Omega\cup\Omega_\tau \tag{4}$$

$$\mathscr{M}(\mathbf{Q})(\mathbf{x}) \equiv -\int_{\Omega\cup\Omega_\tau} [\mathbf{Q}(\mathbf{x},\mathbf{y}) + \mathbf{Q}(\mathbf{y},\mathbf{x})] \cdot \boldsymbol{\beta}(\mathbf{x},\mathbf{y})\, \mathrm{d}V_{\mathrm{y}} \qquad \text{for } \mathbf{x} \in \Omega_\tau \tag{5}$$

in which $\mathbf{Q}(\mathbf{x},\mathbf{y})$ is a tensor function between point $\mathbf{x}$ and point $\mathbf{y}$; $\mathbf{P}(\mathbf{y})$ is a vector function of point $\mathbf{y}$. $\boldsymbol{\beta}(\mathbf{x},\mathbf{y})$ is given as follows:

$$\boldsymbol{\beta}(\mathbf{x},\mathbf{y}) = \frac{\mathbf{x}-\mathbf{y}}{|\mathbf{y}-\mathbf{x}|} \tag{6}$$

$\Gamma(\mathbf{x},\mathbf{y})$ in Eqs. (1) and (4) is related to the nonlocal weighting function $\varpi(\mathbf{x},\mathbf{y})$ in Eq. (1):

$$\Gamma(\mathbf{x},\mathbf{y}) = \frac{|\mathbf{y}-\mathbf{x}|\,\varpi(\mathbf{x},\mathbf{y})}{\psi(\mathbf{x})} \tag{7}$$

in which $\psi(\mathbf{x})$ is dependent on the material parameters $\varphi(\mathbf{x})$ and $\chi(\mathbf{x})$. In the three dimensional problem, material parameters $\varphi(\mathbf{x})$ and $\chi(\mathbf{x})$ in Eq. (1) are expressed as

$$\chi(\mathbf{x}) = \kappa - \frac{\varphi(\mathbf{x})\,\psi(\mathbf{x})}{3} \qquad \psi(\mathbf{x}) = \frac{1}{3}\overline{m}(\mathbf{x}) \qquad \varphi(\mathbf{x}) = \frac{15\mu}{\overline{m}(\mathbf{x})} \tag{8}$$

where μ denotes shear modulus; κ denotes bulk modulus; and $\overline{m}$ is

$$\overline{m}(\mathbf{x}) = \int_{\Omega\cup\Omega_\tau} |\mathbf{y}-\mathbf{x}|^2 \varpi(\mathbf{x},\mathbf{y})\, \mathrm{d}V_{\mathrm{y}} \tag{9}$$

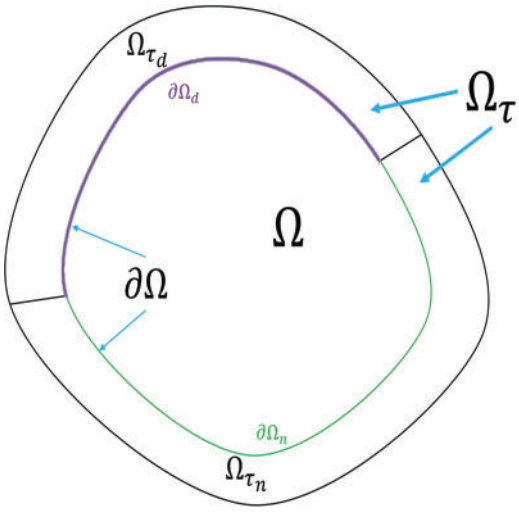

Figure 1: The diagram for volume-constrained boundary (color online)

For the two-dimensional problem, material parameters $\varphi(\mathbf{x})$ and $\chi(\mathbf{x})$ in Eq. (1) are expressed as

$$\chi(\mathbf{x}) = \kappa - \frac{\varphi(\mathbf{x})\,\psi(\mathbf{x})}{2} \qquad \psi(\mathbf{x}) = \frac{1}{2}\overline{m}(\mathbf{x}) \qquad \varphi(\mathbf{x}) = \frac{8\mu}{\overline{m}(\mathbf{x})} \tag{10}$$

It is noteworthy that the literature [5,43] also give the similar nonlocal operators. The connection of both nonlocal operators is in Appendix A.

Stemming from simplifying form, we introduce the following notations:

$$\mathscr{G}(\mathbf{u})(\mathbf{x}) = \mathscr{B}\left(\varphi\varpi\left(\mathscr{B}^*(\mathbf{u})\right)^{\mathrm{T}} + \Gamma\chi\,\mathscr{T}_{\mathrm{r}}\left(\mathscr{B}^*_{\Gamma}(\mathbf{u})\right)\mathbf{I}\right)(\mathbf{x}) \tag{11}$$

$$\mathscr{M}\left(\mathbf{u}\right)\left(\mathbf{x}\right)=\mathscr{M}\left(\varphi\varpi\left(\mathscr{B}^{*}\left(\mathbf{u}\right)\right)^{\mathrm{T}}+\Gamma\chi\mathscr{T}_{\mathrm{r}}\left(\mathscr{B}_{\Gamma}^{*}\left(\mathbf{u}\right)\right)\mathbf{I}\right)\left(\mathbf{x}\right) \tag{12}$$

For two instances with different body forces and boundary constraints, Eq. (1) can be rewritten as

$$Instance1:\begin{cases}\mathscr{G}\left(\mathbf{v}_{1}\right)\left(\mathbf{x}\right)+\mathbf{F}_{\mathrm{b}1}\left(\mathbf{x}\right)=\mathbf{0} & \text{for } \mathbf{x}\in\Omega\\ \mathbf{v}_{1}\left(\mathbf{x}\right)=\mathbf{h}_{\mathrm{u}1}\left(\mathbf{x}\right) & \text{for } \mathbf{x}\in\Omega_{\tau_{d}}\\ \mathscr{M}\left(\mathbf{v}_{1}\right)\left(\mathbf{x}\right)=\mathbf{g}_{\sigma 1}\left(\mathbf{x}\right) & \text{for } \mathbf{x}\in\Omega_{\tau_{n}}\end{cases} \tag{13}$$

$$Instance2:\begin{cases}\mathscr{G}\left(\mathbf{v}_{2}\right)\left(\mathbf{x}\right)+\mathbf{F}_{\mathrm{b}2}\left(\mathbf{x}\right)=\mathbf{0} & \text{for } \mathbf{x}\in\Omega\\ \mathbf{v}_{2}\left(\mathbf{x}\right)=\mathbf{h}_{\mathrm{u}2}\left(\mathbf{x}\right) & \text{for } \mathbf{x}\in\Omega_{\tau_{d}}\\ \mathscr{M}\left(\mathbf{v}_{2}\right)\left(\mathbf{x}\right)=\mathbf{g}_{\sigma 2}\left(\mathbf{x}\right) & \text{for } \mathbf{x}\in\Omega_{\tau_{n}}\end{cases} \tag{14}$$

Following the derivations of the reciprocal theorem of the BBPD in [21], we can obtain the reciprocal theorem for OSPD

$$\begin{aligned}&\int_{\Omega}\mathbf{v}_{2}\left(\mathbf{x}\right)\cdot\mathscr{G}\left(\mathbf{v}_{1}\right)\left(\mathbf{x}\right)\mathrm{d}V_{\mathbf{x}}-\int_{\Omega}\mathbf{v}_{1}\left(\mathbf{x}\right)\cdot\mathscr{G}\left(\mathbf{v}_{2}\right)\left(\mathbf{x}\right)\mathrm{d}V_{\mathbf{x}}\\&=\int_{\Omega_{\tau}}\mathbf{v}_{2}\left(\mathbf{x}\right)\cdot\mathscr{M}\left(\mathbf{v}_{1}\right)\left(\mathbf{x}\right)\mathrm{d}V_{\mathbf{x}}-\int_{\Omega_{\tau}}\mathbf{v}_{1}\left(\mathbf{x}\right)\cdot\mathscr{M}\left(\mathbf{v}_{2}\right)\left(\mathbf{x}\right)\mathrm{d}V_{\mathbf{x}}\end{aligned} \tag{15}$$

whose form is consistent with that of bond-based PD except for the operators defined in Eqs. (13) and (14). The integrals on the left side and right one respectively denote internal integrals and volume-constrained boundary integrals. One can find that the boundary integrals are also volume integrals, which deprives the advantage of the dimensionality reduction for the BEM. Thus we introduce an extra condition to the volume-constrained boundary, which converts the integral on the right side of Eq. (15) from the one in the volume-constrained boundary to the one on the local boundary. The equivalency relationship to transform the integral in volume-constrained boundary Ω_{τ} into the one on local boundary $\partial\Omega$ is

$$\int_{\Omega_{\tau}}\mathbf{u}_{s}\left(\mathbf{x}\right)\cdot\mathscr{M}\left(\mathbf{u}\right)\left(\mathbf{x}\right)\mathrm{d}V_{\mathbf{x}}=\int_{\partial\Omega}\mathbf{u}_{s}\left(\mathbf{x}\right)\cdot\overline{\mathbf{T}}\left(\mathbf{u}\right)\left(\mathbf{x},\mathbf{n}\right)\mathrm{d}V_{\mathbf{x}} \tag{16}$$

where $\mathbf{u}$ is authentic displacement state, it meets Eq. (1). $\mathbf{u}_{s}$ is a possible displacement state, it satisfies displacement constraint in Eq. (1):

$$\mathbf{u}_{s}\left(\mathbf{x}\right)=\mathbf{h}_{\mathrm{u}}\left(\mathbf{x}\right)\qquad\text{for } \mathbf{x}\in\Omega_{\tau_{d}} \tag{17}$$

$\overline{\mathbf{T}}$ is the PD force flux vector operator [44,45], and $\mathbf{n}$ denotes the outward-directed unit normal vector for the point $\mathbf{x}$ that is located on the classical local boundary $\partial\Omega$. $\overline{\mathbf{T}}\left(\mathbf{v}\right)\left(\mathbf{x},\mathbf{n}\right)$ represents the PD force flux vector of the deformed state $\mathbf{v}$ for the point $\mathbf{x}$ in direction $\mathbf{n}$, which is defined as follows [44]:

$$\overline{\mathbf{T}}\left(\mathbf{v}\right)\left(\mathbf{x},\mathbf{n}\right)=\frac{1}{2}\int_{\mathscr{O}}\int_{0}^{+\infty}\int_{0}^{+\infty}\left(y+z\right)^{2}\mathbf{f}\left(\mathbf{x}+y\mathbf{k},\mathbf{v}\left(\mathbf{x}+y\mathbf{k}\right),\mathbf{x}-z\mathbf{k},\mathbf{v}\left(\mathbf{x}-z\mathbf{k}\right)\right)\otimes\mathbf{k}\cdot\mathbf{n}\mathrm{d}z\mathrm{d}y\mathrm{d}\Omega_{m} \tag{18}$$

where $\mathscr{O}$ denotes unit spherical surface; $\mathbf{k}$ denotes unit normal vector of the unit spherical surface $\mathscr{O}$; $\mathrm{d}\Omega_{m}$ is differential solid angle on the surface $\mathscr{O}$ in direction $\mathbf{k}$. $\mathbf{f}\left(\mathbf{x}+y\mathbf{k},\mathbf{v}\left(\mathbf{x}+y\mathbf{k}\right),\mathbf{x}-z\mathbf{k},\mathbf{v}\left(\mathbf{x}-z\mathbf{k}\right)\right)$ denotes response function between point $\mathbf{x}+y\mathbf{k}$ and point $\mathbf{x}-z\mathbf{k}$ [34], which is given as follows:

$$\mathbf{f}\left(\mathbf{x}+y\mathbf{k},\mathbf{v}\left(\mathbf{x}+y\mathbf{k}\right),\mathbf{x}-z\mathbf{k},\mathbf{v}\left(\mathbf{x}-z\mathbf{k}\right)\right)=\mathbf{K}_{c}\left(\mathbf{x}+y\mathbf{k},\mathbf{x}-z\mathbf{k}\right)\cdot\left(\mathbf{v}\left(\mathbf{x}-z\mathbf{k}\right)-\mathbf{v}\left(\mathbf{x}+y\mathbf{k}\right)\right) \tag{19}$$

where $\mathbf{K}_{c}\left(\mathbf{x}+y\mathbf{k},\mathbf{x}-z\mathbf{k}\right)$ is the micromodulus tensor for the linear elastic OSPD [34]. We know that $\mathscr{M}\left(\mathbf{v}\right)\left(\mathbf{x}\right)$ on left side of Eq. (16) is analogous to body force density in Ω_{τ}, and $\overline{\mathbf{T}}\left(\mathbf{v}\right)\left(\mathbf{x},\mathbf{n}\right)$ on right side

of Eq. (16) is analogous to surface traction on $\partial\Omega$. As a result, the equivalency relationship in Eq. (16) is perceived as a virtual work principle that is connected with possible deformed state $\mathbf{u}_s$. Applying $\mathbf{u}_s = \mathbf{v}_1, \mathbf{u} = \mathbf{v}_2$ and $\mathbf{u}_s = \mathbf{v}_2, \mathbf{u} = \mathbf{v}_1$ to Eq. (16) respectively, one can obtain the following two equations:

$$\int_{\Omega_\tau} \mathbf{v}_1(\mathbf{x}) \cdot \mathscr{M}(\mathbf{v}_2)(\mathbf{x})\, \mathrm{d}V_{\mathbf{x}} = \int_{\partial\Omega} \mathbf{v}_1(\mathbf{x}) \cdot \overline{\mathbf{T}}(\mathbf{v}_2)(\mathbf{x}, \mathbf{n})\, \mathrm{d}V_{\mathbf{x}} \tag{20}$$

$$\int_{\Omega_\tau} \mathbf{v}_2(\mathbf{x}) \cdot \mathscr{M}(\mathbf{v}_1)(\mathbf{x})\, \mathrm{d}V_{\mathbf{x}} = \int_{\partial\Omega} \mathbf{v}_2(\mathbf{x}) \cdot \overline{\mathbf{T}}(\mathbf{v}_1)(\mathbf{x}, \mathbf{n})\, \mathrm{d}V_{\mathbf{x}} \tag{21}$$

Substituting Eqs. (20) and (21) into Eq. (15), the reciprocal theorem is rewritten as

$$\begin{aligned} &\int_{\Omega} \mathbf{v}_2(\mathbf{x}) \cdot \mathscr{G}(\mathbf{v}_1)(\mathbf{x})\, \mathrm{d}V_{\mathbf{x}} - \int_{\Omega} \mathbf{v}_1(\mathbf{x}) \cdot \mathscr{G}(\mathbf{v}_2)(\mathbf{x})\, \mathrm{d}V_{\mathbf{x}} \\ &= \int_{\partial\Omega} \mathbf{v}_2(\mathbf{x}) \cdot \overline{\mathbf{T}}(\mathbf{v}_1)(\mathbf{x}, \mathbf{n}) - \mathbf{v}_1(\mathbf{x}) \cdot \overline{\mathbf{T}}(\mathbf{v}_2)(\mathbf{x}, \mathbf{n})\, \mathrm{d}V_{\mathbf{x}} \end{aligned} \tag{22}$$

which builds up a connection between internal integrals and classical boundary integrals, and is a precondition of BIE that will be derived as follows.

Imitating opinion in traditional BEM [46]. We take into account *Problem* 1 corresponding to the actual problem in the reciprocal theorem, and *Problem* 2 denotes infinite domain Green's function $\mathbf{u}_G$ [35], Then, based on the Eq. (1), equilibrium equations corresponding to *Problem* 1 and *Problem* 2 are respectively described as

$$\text{Problem 1}: \begin{cases} \mathscr{G}(\mathbf{u})(\mathbf{x}) + \mathbf{F}_{\mathrm{b}}(\mathbf{x}) = \mathbf{0} & \text{for } \mathbf{x} \in \Omega \\ \mathbf{u}(\mathbf{x}) = \mathbf{h}_{\mathrm{u}}(\mathbf{x}) & \text{for } \mathbf{x} \in \Omega_{\tau_d} \\ \mathscr{M}(\mathbf{u})(\mathbf{x}) = \mathbf{g}_{\sigma}(\mathbf{x}) & \text{for } \mathbf{x} \in \Omega_{\tau_n} \end{cases} \tag{23}$$

$$\text{Problem 2}: \begin{cases} \mathscr{G}(\mathbf{u}_G)(\mathbf{x} - \overline{\mathbf{x}}_m) + \Xi(\mathbf{x} - \overline{\mathbf{x}}_m)\mathbf{E}_i = \mathbf{0} & \text{for } \mathbf{x} \in \Omega \\ \mathbf{u}_G(\mathbf{x} - \overline{\mathbf{x}}_m) = \overline{\mathbf{u}}_G(\mathbf{x} - \overline{\mathbf{x}}_m) & \text{for } \mathbf{x} \in \Omega_{\tau_d} \\ \mathscr{M}(\mathbf{u}_G)(\mathbf{x} - \overline{\mathbf{x}}_m) = \mathscr{M}(\overline{\mathbf{u}}_G)(\mathbf{x} - \overline{\mathbf{x}}_m) & \text{for } \mathbf{x} \in \Omega_{\tau_n} \end{cases} \tag{24}$$

where $\mathbf{E}_i$ denotes a coordinate axis vector. $\overline{\mathbf{u}}_G$ meets

$$\mathscr{G}(\overline{\mathbf{u}}_G)(\mathbf{x} - \overline{\mathbf{x}}_m) + \Xi(\mathbf{x} - \overline{\mathbf{x}}_m)\mathbf{E}_i = \mathbf{0} \qquad \text{for } \overline{\mathbf{x}}_m \in \Omega, \mathbf{x} \in \mathbb{R}^{\mathrm{n}} \tag{25}$$

where $\Xi(\mathbf{x} - \overline{\mathbf{x}}_m)$ is Dirac function; $\mathbb{R}^{\mathrm{n}}$ dentes the n-dimensional infinite Euclidean space. Substituting $\mathbf{v}_1 = \mathbf{u}_G$ and $\mathbf{v}_2 = \mathbf{u}$ into Eq. (22), we obtain

$$\begin{aligned} &\int_{\Omega} \mathbf{u}(\mathbf{x}) \cdot \mathscr{G}(\mathbf{u}_G)(\mathbf{x} - \overline{\mathbf{x}}_m)\, \mathrm{d}V_{\mathbf{x}} - \int_{\Omega} \mathbf{u}_G(\mathbf{x} - \overline{\mathbf{x}}_m) \cdot \mathscr{G}(\mathbf{u})(\mathbf{x})\, \mathrm{d}V_{\mathbf{x}} \\ &= \int_{\partial\Omega} \mathbf{u}(\mathbf{x}) \cdot \overline{\mathbf{T}}(\mathbf{u}_G)(\mathbf{x} - \overline{\mathbf{x}}_m, \mathbf{n}) - \mathbf{u}_G(\mathbf{x} - \overline{\mathbf{x}}_m) \cdot \overline{\mathbf{T}}(\mathbf{u})(\mathbf{x}, \mathbf{n})\, \mathrm{d}V_{\mathbf{x}} \end{aligned} \tag{26}$$

Applying first equations for Eqs. (23) and (24) to (26), we obtain

$$\begin{aligned} &\int_{\Omega} \mathbf{u}(\mathbf{x}) \cdot (-\Xi(\mathbf{x} - \overline{\mathbf{x}}_m)\mathbf{E}_i)\, \mathrm{d}V_{\mathbf{x}} + \int_{\Omega} \mathbf{u}_G(\mathbf{x} - \overline{\mathbf{x}}_m) \cdot \mathbf{F}_{\mathrm{b}}(\mathbf{x})\, \mathrm{d}V_{\mathbf{x}} \\ &= \int_{\partial\Omega} \mathbf{u}(\mathbf{x}) \cdot \overline{\mathbf{T}}(\mathbf{u}_G)(\mathbf{x} - \overline{\mathbf{x}}_m, \mathbf{n}) - \mathbf{u}_G(\mathbf{x} - \overline{\mathbf{x}}_m) \cdot \overline{\mathbf{T}}(\mathbf{u})(\mathbf{x}, \mathbf{n})\, \mathrm{d}V_{\mathbf{x}} \end{aligned} \tag{27}$$

Executing limit analysis $\overline{\mathbf{x}}_m \rightarrow \partial\Omega$ concerning Eq. (27) for acquiring BIE for the OSPD. This process is shown graphically in Fig. 2 in a two-dimensional problem, while the three-dimensional problem is similar. A detailed explanation is in the literature [21]. The result is displayed as follows:

$$\begin{aligned}
&\lim_{\varepsilon\to 0}\left(\int_{\Omega+\Omega_s}\mathbf{u}\left(\mathbf{x}\right)\cdot\left(-\Xi\left(\mathbf{x}-\overline{\mathbf{x}}_m\right)\mathbf{E}_i\right)\mathrm{d}V_{\mathbf{x}}\right)+\int_{\Omega+\Omega_s}\mathbf{u}_G\left(\mathbf{x}-\overline{\mathbf{x}}_m\right)\cdot\mathbf{F}_{\mathrm{b}}\left(\mathbf{x}\right)\mathrm{d}V_{\mathbf{x}}\\
&=\lim_{\varepsilon\to 0}\left(\int_{\partial\Omega-S}\mathbf{u}\left(\mathbf{x}\right)\cdot\overline{\mathbf{T}}\left(\mathbf{u}_G\right)\left(\mathbf{x}-\overline{\mathbf{x}}_m,\mathbf{n}\right)-\mathbf{u}_G\left(\mathbf{x}-\overline{\mathbf{x}}_m\right)\cdot\overline{\mathbf{T}}\left(\mathbf{u}\right)\left(\mathbf{x},\mathbf{n}\right)\mathrm{d}V_{\mathbf{x}}\right)\\
&\quad+\lim_{\varepsilon\to 0}\left(\int_{S^+}\mathbf{u}\left(\mathbf{x}\right)\cdot\overline{\mathbf{T}}\left(\mathbf{u}_G\right)\left(\mathbf{x}-\overline{\mathbf{x}}_m,\mathbf{n}\right)-\mathbf{u}_G\left(\mathbf{x}-\overline{\mathbf{x}}_m\right)\cdot\overline{\mathbf{T}}\left(\mathbf{u}\right)\left(\mathbf{x},\mathbf{n}\right)\mathrm{d}V_{\mathbf{x}}\right)
\end{aligned}\tag{28}$$

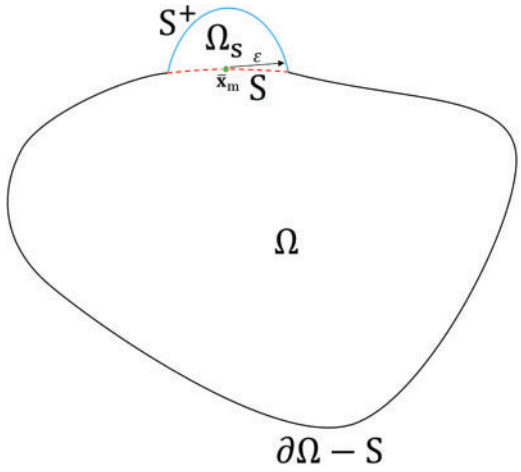

Figure 2: The diagram for the boundary limit process [21] (color online)

The result for the integral on left side of Eq. (28) is $-\mathbf{u}_k\left(\overline{\mathbf{x}}_m\right)$ due to property of Dirac function. The result for the first item on the right side of Eq. (28) equals to Cauchy principal value (CPV) of integral on $\partial\Omega$. The result for the second item on the right side of Eq. (28) involves analyzing singularity for integrand. The singularity for integrand exists in Green's function $\mathbf{u}_G$. According to the literature [35], the logarithmic and Dirac singularity are involved. The integrable property of logarithmic singularity and the convolution property of the Dirac function cause the result for the second item on the right side of Eq. (28) to vanish. Then, Eq. (28) is given as below:

$$-\mathbf{u}_k\left(\overline{\mathbf{x}}_m\right)+\int_{\Omega}\mathbf{u}_G\left(\mathbf{x}-\overline{\mathbf{x}}_m\right)\cdot\mathbf{F}_{\mathrm{b}}\left(\mathbf{x}\right)\mathrm{d}V_{\mathbf{x}}=\int_{\partial\Omega}\mathbf{u}\left(\mathbf{x}\right)\cdot\overline{\mathbf{T}}\left(\mathbf{u}_G\right)\left(\mathbf{x}-\overline{\mathbf{x}}_m,\mathbf{n}\right)-\mathbf{u}_G\left(\mathbf{x}-\overline{\mathbf{x}}_m\right)\cdot\overline{\mathbf{T}}\left(\mathbf{u}\right)\left(\mathbf{x},\mathbf{n}\right)\mathrm{d}V_{\mathbf{x}}\tag{29}$$

where $\int$ is CPV for integral. Dividing $\partial\Omega$ into $\partial\Omega_n$ and $\partial\Omega_d$, Eq. (29) can be rewritten as

$$\begin{aligned}
\mathbf{u}_k\left(\overline{\mathbf{x}}_m\right)=&-\int_{\partial\Omega_d}\mathbf{u}\left(\mathbf{x}\right)\cdot\overline{\mathbf{T}}\left(\mathbf{u}_G\right)\left(\mathbf{x}-\overline{\mathbf{x}}_m,\mathbf{n}\right)-\mathbf{u}_G\left(\mathbf{x}-\overline{\mathbf{x}}_m\right)\cdot\overline{\mathbf{T}}\left(\mathbf{u}\right)\left(\mathbf{x},\mathbf{n}\right)\mathrm{d}V_{\mathbf{x}}+\int_{\Omega}\mathbf{u}_G\left(\mathbf{x}-\overline{\mathbf{x}}_m\right)\cdot\mathbf{F}_{\mathrm{b}}\left(\mathbf{x}\right)\mathrm{d}V_{\mathbf{x}}\\
&-\int_{\partial\Omega_n}\mathbf{u}\left(\mathbf{x}\right)\cdot\overline{\mathbf{T}}\left(\mathbf{u}_G\right)\left(\mathbf{x}-\overline{\mathbf{x}}_m,\mathbf{n}\right)-\mathbf{u}_G\left(\mathbf{x}-\overline{\mathbf{x}}_m\right)\cdot\overline{\mathbf{T}}\left(\mathbf{u}\right)\left(\mathbf{x},\mathbf{n}\right)\mathrm{d}V_{\mathbf{x}}
\end{aligned}\tag{30}$$

Adopting an approach in the literature [47,48] to build up a relation between PD boundary constraints and local boundary constraints, we obtain the following relationship:

$$\mathbf{u}(\mathbf{x}) = \hat{\mathbf{v}}(\mathbf{x}) \qquad \mathbf{x} \in \partial\Omega_d \tag{31}$$

$$\overline{\mathbf{T}}(\mathbf{u})(\mathbf{x}, \mathbf{n}) = \boldsymbol{\tau}_f(\mathbf{x}) \qquad \mathbf{x} \in \partial\Omega_n \tag{32}$$

where $\hat{\mathbf{v}}(\mathbf{x})$ and $\boldsymbol{\tau}_f(\mathbf{x})$ are the local boundary condition. Putting Eqs. (31) and (32) into Eq. (30) generates

$$\begin{aligned}\mathbf{u}_k(\overline{\mathbf{x}}_m) = &-\int_{\partial\Omega_d} \hat{\mathbf{v}}(\mathbf{x}) \cdot \overline{\mathbf{T}}(\mathbf{u}_G)(\mathbf{x} - \overline{\mathbf{x}}_m, \mathbf{n}) - \mathbf{u}_G(\mathbf{x} - \overline{\mathbf{x}}_m) \cdot \overline{\mathbf{T}}(\mathbf{u})(\mathbf{x}, \mathbf{n})\, \mathrm{d}V_{\mathbf{x}} + \int_{\Omega} \mathbf{u}_G(\mathbf{x} - \overline{\mathbf{x}}_m) \cdot \mathbf{F}_{\mathrm{b}}(\mathbf{x})\, \mathrm{d}V_{\mathbf{x}} \\ &-\int_{\partial\Omega_n} \mathbf{u}(\mathbf{x}) \cdot \overline{\mathbf{T}}(\mathbf{u}_G)(\mathbf{x} - \overline{\mathbf{x}}_m, \mathbf{n}) - \mathbf{u}_G(\mathbf{x} - \overline{\mathbf{x}}_m) \cdot \boldsymbol{\tau}_f(\mathbf{x})\, \mathrm{d}V_{\mathbf{x}}\end{aligned} \tag{33}$$

which is the BIE of OSPD for the static case. For the dynamic case, we give BIE corresponding to the Laplace domain in Appendix B. Once a displacement and force flux on the local boundary $\partial\Omega$ are obtained, one can calculate the displacement of any material point within the domain Ω through the BIE Eqs. (33) and (B.13). Therefore, we just need to calculate the displacement and force on the local boundary through the discretization method in [21]. The details will be repeated. So far, one can use the OSPD-BEM to simulate static and dynamic problems without fracture. For fracture problems, it is essential to research the crack propagation model for any BEM. Therefore, we propose a crack propagation model that is suitable for the present numerical method.

3 Crack Propagation Model

The crack propagation model for the OSPD-BEM proposed in this paper is inspired by the cohesive crack model [29–31] and the PD bilinear model [32,33]. We take a continuum medium in Fig. 3 as an example, and the construction of the model is given as follows.

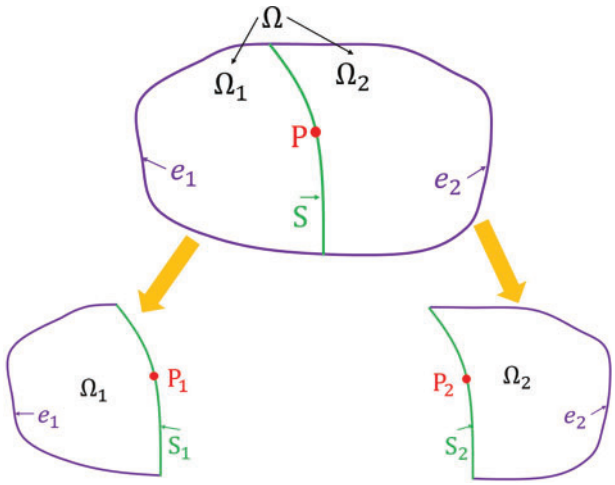

Figure 3: The diagram of the crack propagation model (color online)

In Fig. 3, S is the preset crack propagation path in Ω. Ω is divided into two subdivisions Ω_1 and Ω_2 with a path S. e_1 and S_1 compose the boundary of Ω_1, while e_2 and S_2 compose the boundary of Ω_2. We can convert the process of solving Ω to the process of solving Ω_1 and Ω_2. Therefore, the BIE of the

OSPD Eq. (33) is applied to the boundary $e_1 + S_1$ and the boundary $e_2 + S_2$, respectively. If there is no crack, S_1 and S_2 are the same surface, so the continuity condition should be satisfied on S_1 and S_2. As shown in Fig. 4, for any pair of associated points P_1 and P_2 on S_1 and S_2, the continuity condition is expressed as

$$\overline{\mathbf{T}}_1\left(\mathbf{u}_1\right)\left(\mathbf{x}_{P_1}, \mathbf{n}_{S_1}\right) = -\overline{\mathbf{T}}_2\left(\mathbf{u}_2\right)\left(\mathbf{x}_{P_2}, \mathbf{n}_{S_2}\right) \tag{34}$$

$$\mathbf{u}_1\left(\mathbf{x}_{P_1}\right) = \mathbf{u}_2\left(\mathbf{x}_{P_2}\right) \tag{35}$$

where $\overline{\mathbf{T}}_1\left(\mathbf{u}_1\right)\left(\mathbf{x}_{P_1}, \mathbf{n}_{S_1}\right)$ is the PD force flux vector at the point P_1 on the surface S_1, while $\overline{\mathbf{T}}_2\left(\mathbf{u}_2\right)\left(\mathbf{x}_{P_2}, \mathbf{n}_{S_2}\right)$ is the PD force flux vector at the point P_2 on the surface S_2; $\mathbf{u}_1\left(\mathbf{x}_{P_1}\right)$ is the displacement at the point P_1; $\mathbf{u}_2\left(\mathbf{x}_{P_2}\right)$ is the displacement at the point P_2. We can obtain the PD force flux vector $\overline{\mathbf{T}}_1, \overline{\mathbf{T}}_2$ and the displacement $\mathbf{u}_1, \mathbf{u}_2$ on the preset crack propagation path S by solving the BIE respectively for the boundary $e_1 + S_1$ and the boundary $e_2 + S_2$. Next, we substitute the results of $\overline{\mathbf{T}}_1$, $\overline{\mathbf{T}}_2$, $\mathbf{u}_1$ and $\mathbf{u}_2$ into our crack propagation model to determine whether this material point P is divided into P_1 and P_2.

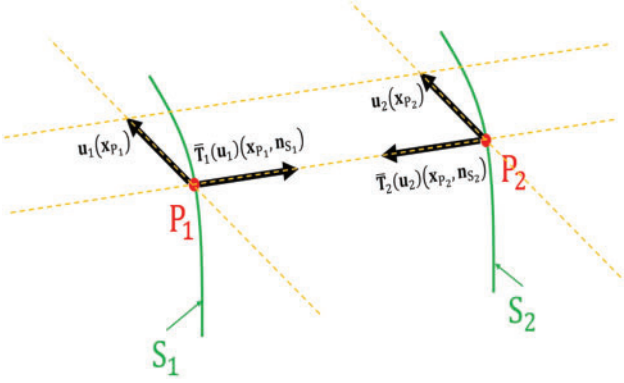

Figure 4: The diagram for the crack propagation model in the elastic stage (color online)

For the crack propagation model, we consider that the fracture at any material point P at the preset crack propagation path is divided into three stages: the elastic stage, the adhesive stage and the defunct stage. The elastic stage is given in Fig. 4, and the calculation can be completed with the continuity condition Eqs. (34) and (35). The defunct stage is given in Fig. 5, and the crack occurs at this time. At the defunct stage, the material point P is divided into P_1 and P_2, and the force flux vectors $\overline{\mathbf{T}}_1$ and $\overline{\mathbf{T}}_2$ vanish. The calculation is also easily completed at this stage. Next, we discuss the complicated adhesive stage in Fig. 6. The adhesive stage needs to answer two problems. One is about the end of the elastic stage and the start of the defunct stage, and the other is about the constitutive relationship between the PD force flux vectors, i.e., $\overline{\mathbf{T}}_1$ and $\overline{\mathbf{T}}_2$, and the displacement vectors, i.e., $\mathbf{u}_1$ and $\mathbf{u}_2$. We start with the problem two. In Fig. 6, the PD force flux vectors $\overline{\mathbf{T}}_1$ and $\overline{\mathbf{T}}_2$ satisfy the equilibrium relationship

$$\overline{\mathbf{T}}_1\left(\mathbf{u}_1\right)\left(\mathbf{x}_{P_1}, \mathbf{n}_{S_1}\right) = -\overline{\mathbf{T}}_2\left(\mathbf{u}_2\right)\left(\mathbf{x}_{P_2}, \mathbf{n}_{S_2}\right) = \overline{\mathbf{T}}\left(\mathbf{x}_{P_1} - \mathbf{x}_{P_2}\right) \tag{36}$$

The force flux vector $\overline{\mathbf{T}}\left(\mathbf{x}_{P_1} - \mathbf{x}_{P_2}\right)$ is related to the relative displacement between the material point P_1 and P_2 which is denoted as

$$\mathbf{u}\left(\mathbf{x}_{P_1} - \mathbf{x}_{P_2}\right) = \mathbf{u}_1\left(\mathbf{x}_{P_1}\right) - \mathbf{u}_2\left(\mathbf{x}_{P_2}\right) \tag{37}$$

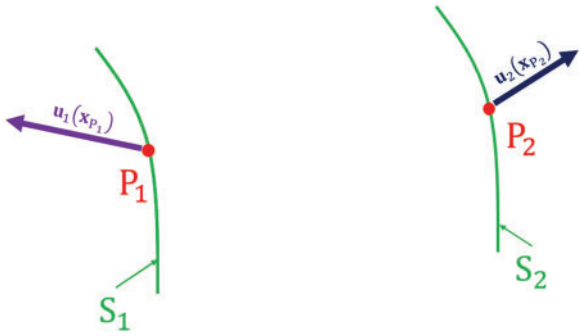

Figure 5: The diagram for the fracture calculation model in the defunct stage (color online)

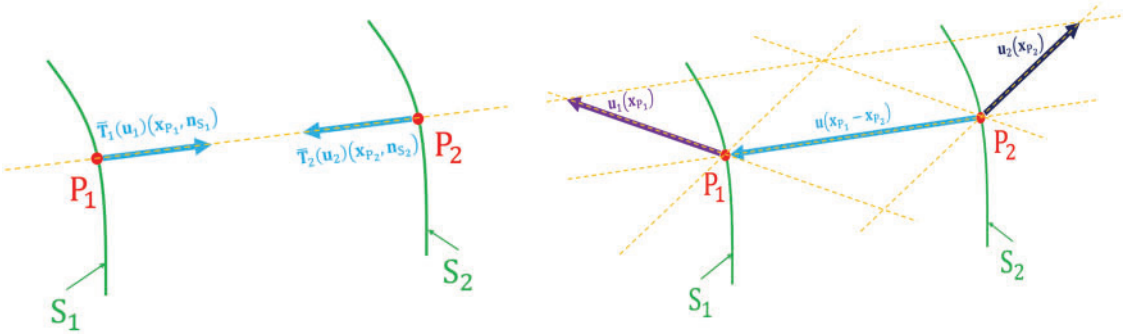

Figure 6: The diagram of the crack propagation model in the adhesive stage (color online)

We assume that the force flux vector $\overline{\mathbf{T}}\left(\mathbf{x}_{P_1} - \mathbf{x}_{P_2}\right)$ and the relative displacement $\mathbf{u}\left(\mathbf{x}_{P_1} - \mathbf{x}_{P_2}\right)$ satisfy the linear relationship shown in Fig. 7. A more complex constitutive relationship, e.g., those in [49,50], can be considered in the future. Next, let's answer the problem one. In Fig. 7, the force flux vector $\overline{\mathbf{T}}_M$ is referred to as the elastic limit flux, and corresponds to the linear elastic stretch limit [32]. According to the article [32,48,51], $\overline{\mathbf{T}}_M$ is expressed as

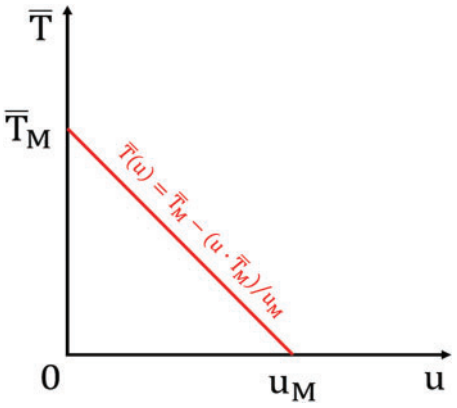

Figure 7: The diagram for the constitutive relationship in the adhesive stage (color online)

$$\overline{\mathbf{T}}_{\mathrm{M}} = \begin{cases} \dfrac{6\pi\kappa}{\mathrm{h_r}}\sqrt{\dfrac{G_0\mathrm{h_r}}{54\pi\mu + 16(\kappa - 2\mu)}} & \text{for 2D} \\ \dfrac{48\kappa}{\mathrm{h_r}}\sqrt{\dfrac{G_0\mathrm{h_r}}{768\mu + 27(3\kappa - 5\mu)}} & \text{for 3D} \end{cases} \tag{38}$$

where μ denotes shear modulus; κ denotes bulk modulus; $\mathrm{h_r}$ is horizon; G_0 is the elastic limit energy density [32]. When $\overline{\mathbf{T}}_{\mathrm{l}}(\mathbf{u}_{\mathrm{l}})\left(\mathbf{x}_{\mathrm{P_l}}, \mathbf{n}_{\mathrm{S_l}}\right)$ in Eq. (34) achieves $\overline{\mathbf{T}}_{\mathrm{M}}$, the elastic stage is ended. $\mathbf{u}_{\mathrm{M}}$ in Fig. 7 is referred to as the adhesive limit displacement, and it is determined by a Law of energy conservation for a process of the new crack growing [52].

$$G_{IC} = G_0 + \frac{1}{2}\overline{\mathbf{T}}_{\mathrm{M}}\mathbf{u}_{\mathrm{M}} \tag{39}$$

where G_{IC} is the critical energy release rate [51]. When $\mathbf{u}\left(\mathbf{x}_{\mathrm{P_1}} - \mathbf{x}_{\mathrm{P_2}}\right)$ in Eq. (37) achieves $\mathbf{u}_{\mathrm{M}}$, the defunct stage is started. The solving procedure of our crack propagation model can be summarized as Fig. 8.

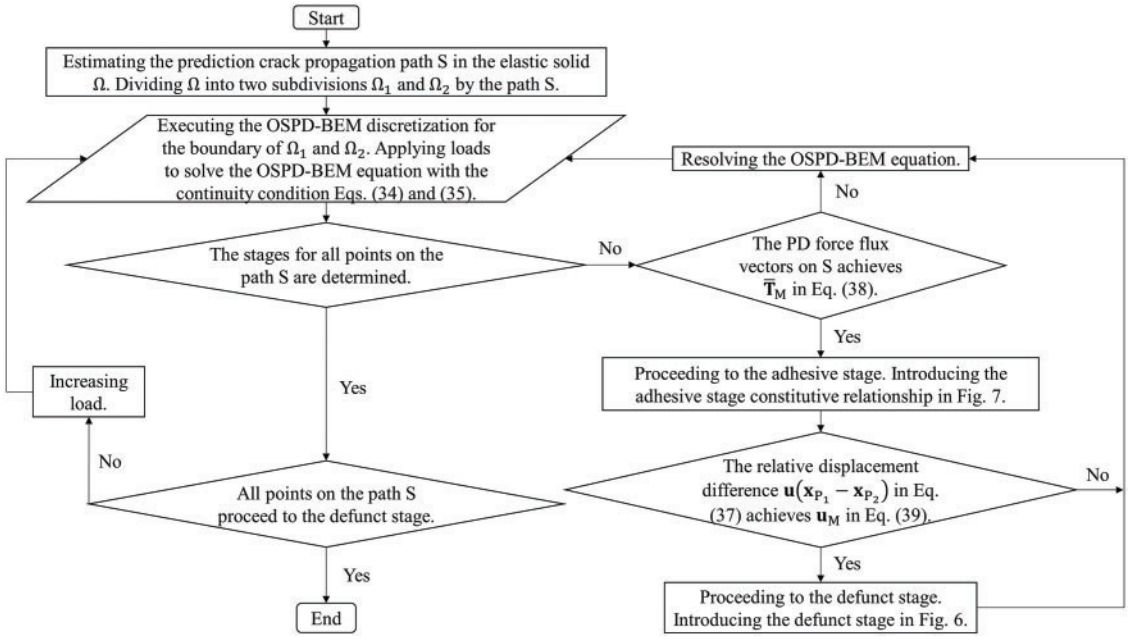

Figure 8: The flow chart for the solving process of the crack propagation model

4 Numerical Examples

We will take four numerical examples to confirm the accuracy and efficiency of OSPD-BEM in this section. Firstly, a two-dimensional square plate under uniaxial loading is investigated to estimate the numerical Poisson's ratio as those in the literature [53,54]. It displays that our numerical method can be more accurate than the PD-MPM. Secondly, we discuss the crack initiation in a double-notched specimen as the literature [21], which reveals the accuracy and efficiency of the OSPD-BEM compared with the PD-MPM. Thirdly, the wedge-splitting test is simulated to research a fracture toughness for the concrete specimen [55,56], and its result is compared to experimental results, which displays again the the accuracy and efficiency of OSPD-BEM. Finally, a three-point bending experiment is executed.

4.1 Two-Dimensional Square Plate under Uniaxial Loading

We consider a two-dimensional square plate withstanding the uniaxial tensile loading in the direction **x**, as displayed in Fig. 9. The calculation parameters can be obtained in Table 2. a denotes length of the sides; h denotes thickness; E denotes elastic modulus; p denotes tensile loading; $\mathrm{h_r}$ denotes horizon; Δ is the grid spacing. For a given Poisson's ratio ν, we can obtain the deformation of the plate, and then calculate the numerical Poisson's ratios $\tilde{\nu}$ which should be consistent with the given Poisson's ratios. However, due to an error in the numerical method, the numerical Poisson's ratio is probably different from the given Poisson's ratio. The error between the two can be used to test the accuracy of one numerical method. Therefore, in this numerical example, we investigate the deformation state of the plate with different Poisson's ratios, i.e., $\nu = 0.1, 0.2, 0.3$. Then the numerical Poisson's ratios $\tilde{\nu}$ is calculated as

$$\tilde{\nu} = \frac{\Delta y_d}{\Delta x_d} \tag{40}$$

where Δy_d is the average absolute value of the displacement in the direction **y** for all discrete material points. Δx_d is the average absolute value of the displacement in the direction **x** for all discrete material points. The numerical Poisson's ratios $\tilde{\nu}$ obtained by OSPD-BEM and PD-MPM are listed in Table 3. The errors between the numerical Poisson's ratios and the given ones are also given in Table 3.

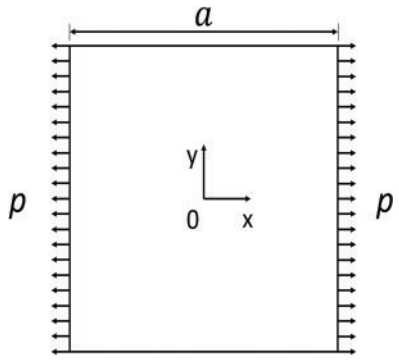

Figure 9: The diagram for stretching square plate

Table 2: Calculation parameters for the stretching square plate

a (m)	h (m)	E (GPa)	p (MPa)	$\mathrm{h_r}$ (m)	Δ (m)
1.0	0.01	200.0	200.0	0.04	0.01

From Table 3, one can find that the errors of the OSPD-BEM are much smaller than those of PD-MPM. Besides, the numerical Poisson's ratios predicted by the PD-MPM are always lower than the given Poisson's ratio, which can be due to a spurious boundary softening phenomena [57]. This phenomenon is observed from the results of PD-MPM in Fig. 10. We find that Poisson's ratio is variable for the OSPD in Table 3, while it is the fixed value for the BBPD. The BBPD-BEM is one order of magnitude more precise than the PD-MPM, while the magnitude is two orders for the OSPD-BEM. The reason is that the spurious boundary softening phenomena [57] is more serious for the OSPD compared with the BBPD.

Table 3: Calculation results for the numerical Poisson's ratios $\tilde{\nu}$

Theory	ν	Boundary element method	Error (%)	PD-MPM	Error (%)
BBPD	1/3	0.333416	0.0248	0.332878	0.1366
OSPD	0.1	0.100087	0.087	0.099146	0.854
	0.2	0.200076	0.038	0.197598	1.201
	0.3	0.300059	0.0196	0.296853	1.049

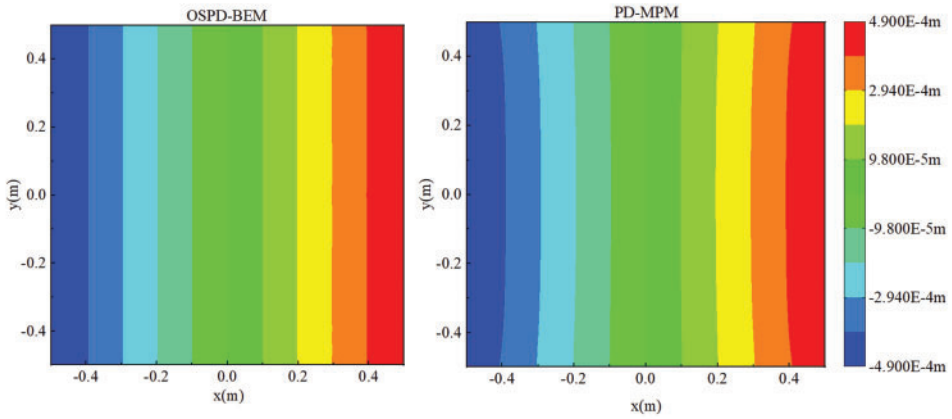

(a) Displacement in the direction **x**

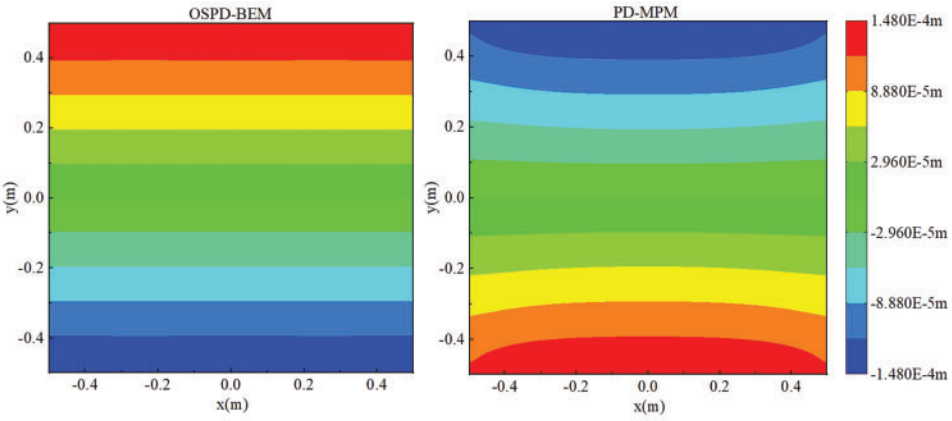

(b) Displacement in the direction **y**

Figure 10: Displacement predicted by the PD-MPM and the OSPD-BEM for $\nu = 0.3$ (color online)

4.2 Two-Dimensional Crack Initiation in a Double-Notched Specimen

In this example, we consider a crack initiation problem in the square plate with a double-notched edge crack exerted uniaxial tensile loading displayed in Fig. 11. The calculation parameters are exhibited in Table 4. E denotes elastic modulus; C_r denotes initial length of the crack; G_c denotes critical energy release rate. According to a definition of critical energy release rate in PD [17], the load corresponding to the crack propagating Δ length is defined as the utmost load F_m. Δ is the grid spacing

[17]. For different Poisson ratios, the results predicted by the OSPD-BEM are compared with those of the PD-MPM.

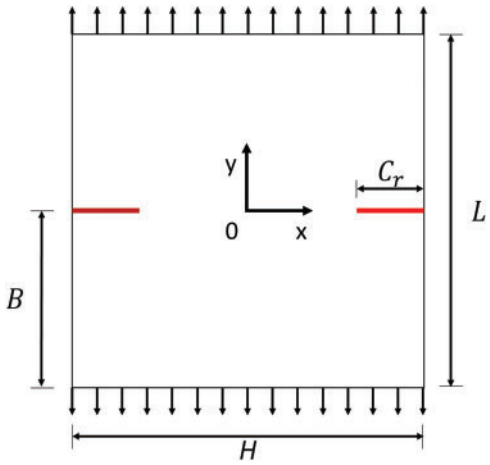

Figure 11: The diagram for a double-notched specimen (color online)

Table 4: Calculation parameters for the double-notched specimen

E (Pa)	C_r (m)	G_c (Pa · m)	L (m)	B (m)	H (m)
1.0	0.1	1.47×10^{-4}	1.0	0.5	1.0

For Poisson's ratio $\nu = 0.3$ and horizon $h_r = 0.0125$ m, the displacements predicted by the OSPD-BEM are compared with those predicted by the PD-MPM in Figs. 12. One can find that both displacements in the direction **x** and **y** are consistent with those predicted by the PD-MPM. But utmost load F_m and calculation time t of both methods are different. For different horizons h_r, the utmost load F_m and the calculation time t predicted by OSPD-BEM and PD-MPM are displayed in Figs. 13 and 14.

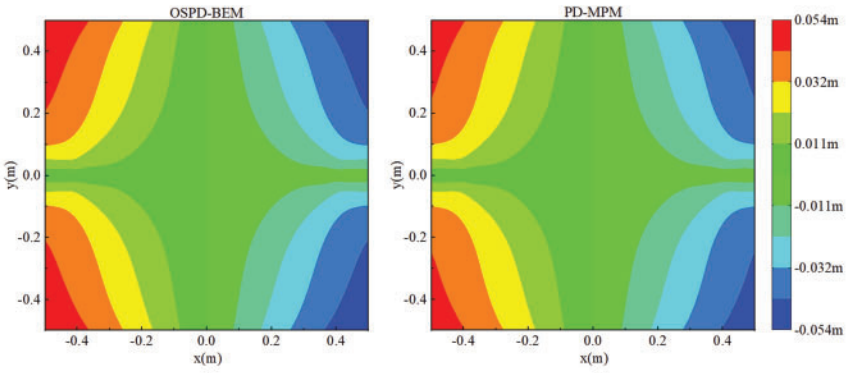

(a) Displacement in the direction **x**

Figure 12: (Continued)

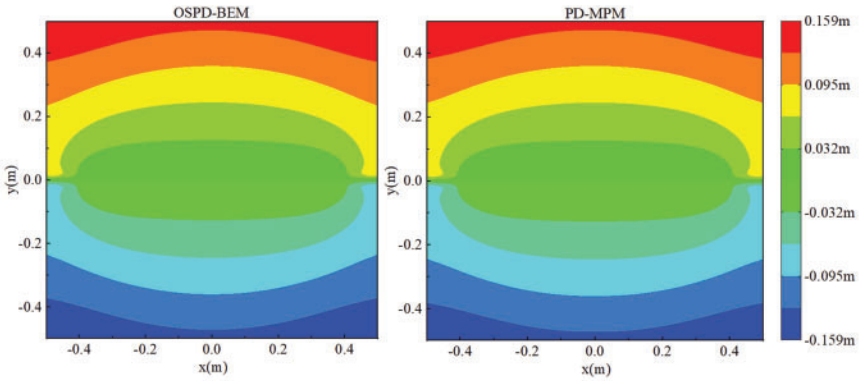

(b) Displacement in the direction **y**

Figure 12: Displacement predicted by the OSPD-BEM and PD-MPM for $\nu = 0.3$ (color online)

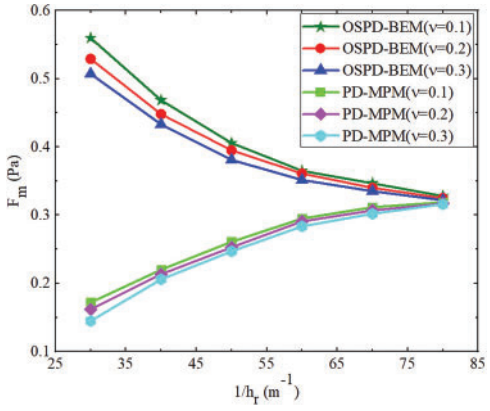

Figure 13: The load F_m *vs*. the reciprocal of the horizon $1/\mathrm{h_r}$ (color online)

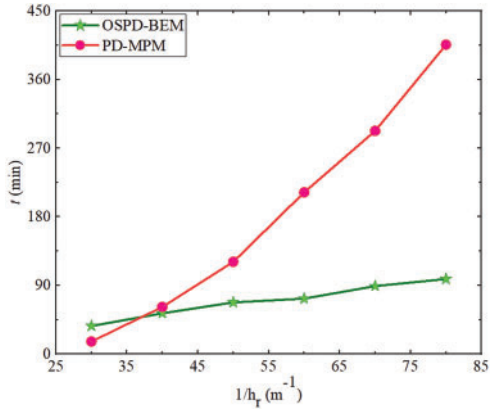

Figure 14: The calculation time t *vs*. the reciprocal of the horizon $1/\mathrm{h_r}$, $\nu = 0.3$ (color online)

In Fig. 13, we find the utmost load F_m acquired through OSPD-BEM can be higher than the one predicted through PD-MPM, and their results are consistent with each other when horizon h_r approaches zero. This phenomenon is consistent with the results in BBPD [21]. The utmost load F_m decreases with an increment of Poisson's ratio, which agrees well with results in this literature [54]. The efficiency is demonstrated in Fig. 14. The calculation time for PD-MPM sharply improves as a reduction of horizon h_r, while the one for OSPD-BEM does not change much. Meanwhile, the asymptotic compatibility [58] has also been demonstrated for the OSPD-BEM.

4.3 Wedge-Splitting Test

The wedge-splitting test is a significant experiment to investigate the fracture toughness of the concrete specimen [55,56]. Many numerical methods based on classical continuum mechanics [59,60] and PD theory [32,61] have been applied to simulate this experiment. In this section, the OSPD-BEM is used to simulate this experiment process, and our result will be compared with those of the ordinary state-based peridynamic mesh-free particle method (OSPD-MPM) predicted by Bie et al. [61]. The schematics of the wedge-splitting test specimen is displayed in Fig. 15. The relative displacement $\bar{\mathbf{u}}$ that is perpendicular to a crack is applied on the pre-cracked edge of a square plate, and hinge supports are applied to the symmetric points on the edge opposite the crack. The geometry and materials parameters are shown in Table 5. E denotes elastic modulus; ν denotes Poisson's ratio; h_r denotes horizon; G_0 denotes elastic limit energy density [32]; G_{IC} denotes critical energy release rate [51]; C_r denotes initial length of a crack.

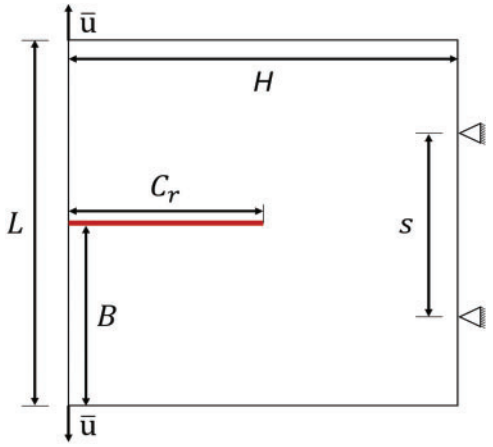

Figure 15: The schematics for the wedge-splitting test specimen (color online)

Table 5: Calculation parameters for the wedge-splitting test

E (GPa)	ν	h_r (m)	G_0 (Pa · m)	G_{IC} (Pa · m)	C_r (m)	L (m)	B (m)	H (m)	s (m)
28.3	0.2	0.128	24.5	490	1.6	3.2	1.6	3.2	1.6

To describe the propagation process of a crack, the curve of the crack length *vs*. the crack mouth opening displacement (CMOD) is given in Fig. 16. Some specific crack propagation diagrams are shown in Fig. 17. The main purpose of the wedge-splitting test is to obtain the curve about the external

load *vs*. CMOD. This curve is related to the fracture toughness of a concrete specimen [55]. Drawing upon the crack propagation model of the OSPD-BEM in Section 3, the curve of the load *vs*. the CMOD is given in Fig. 18. In Fig. 18, we find the result of the OSPD-BEM is closer to the experimental result [56] than the one of PD-MPM in [61]. The reasons originate from two aspects. First, the OSPD-BEM is more accurate as a semi-analytical calculation method. Second, the softening process observed in the test [60,62] is introduced into the crack propagation model.

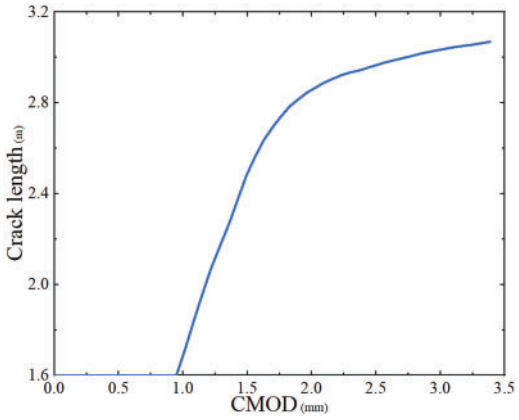

Figure 16: The crack length *vs*. the CMOD (color online)

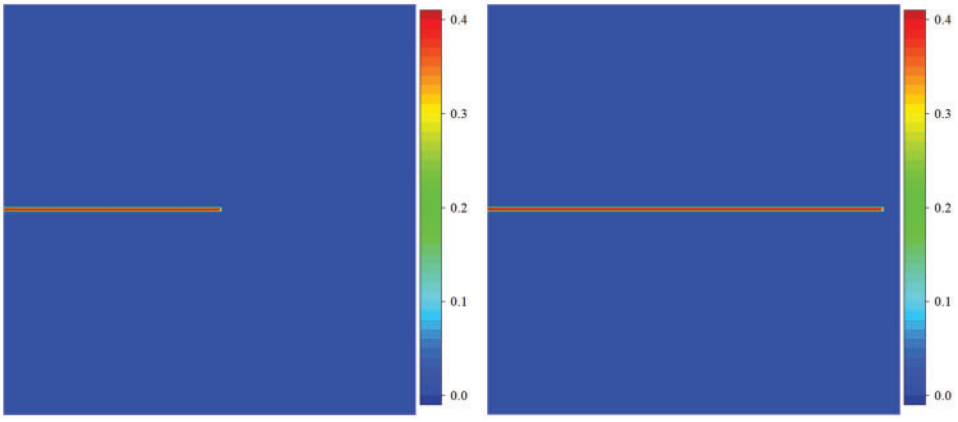

(a) The CMOD is 1.0mm (b) The CMOD is 3.4mm

Figure 17: The crack propagation diagram (color online)

The crack initiation load F_m (i.e., the peak value in Fig. 18) and its corresponding CMOD U_m are significant parameters for the fracture toughness of the concrete specimen. We further compare the fracture toughness predicted by our OSPD-BEM and Bie et al. [61] with the experimental results in Table 6. The error is calculated based on the experimental result [56]. In Table 6, the accuracies of F_m and U_m are respectively improved by one time and seven times when we compare the OSPD-BEM and Bie et al. [61] with the experimental result [56].

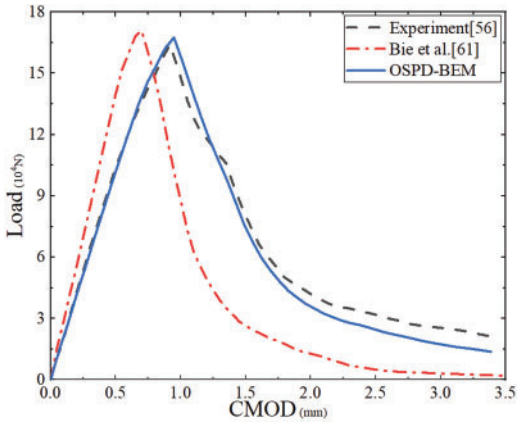

Figure 18: The load *vs*. the CMOD (color online)

Table 6: Fracture toughness comparison

	Experimental result [56]	Bie et al. [61]	Error (%)	OSPD-BEM	Error (%)
F_m (kN)	164.0	171.0	4.27	167.5	2.134
U_m (mm)	0.92	0.7	23.9	0.95	3.26

Considering the calculation efficiency, we find that it takes 44000 s to simulate the wedge-splitting test in Fig. 15 with the OSPD-MPM [61], while the time consumption has been reduced to 21000 s with the coupling method [61] between the OSPD-MPM and the node-based smoothed finite element method (NS-FEM). Nevertheless, the OSPD-BEM only takes 11000 s to deal with the same problem in Fig. 15. The calculation efficiency is respectively improved by three times and one time compared with the OSPD-MPM [61] and the coupling method [61]. By the way, 200 boundary elements are used in the OSPD-BEM for the simulation result in Fig. 15. The computer equipment is displayed as (1) CPU: 12th Gen Intel(R) Core(TM) i5-1240P 1.70 GHz; (2) RAM: 16.0 GB; (3) OS: Windows 11 Home 22H2 64 bit.

4.4 Three Point Bending Test

The three-point bending experiment is the main experimental approach to measure the mechanical properties of materials [63,64]. The beam with a central crack is executed by the three-point bending experimental to investigate fracture toughness in Fig. 19. As displayed in Fig. 19, $\bar{\mathbf{u}}$ represents displacement loading, while the hinge support and the fixed support are applied to both ends of the beam.

The geometry and materials parameters are shown in Table 7. In Table 7, E denotes elastic modulus; ν denotes Poisson's ratio; h_r denotes horizon; G_0 denotes elastic limit energy density [32]; G_{IC} denotes critical energy release rate [51]; C_r denotes initial length of crack. The three-point bending experiment in Fig. 19 is simulated with a crack propagation model of OSPD-BEM in Section 3. To describe the propagation process of the crack, the curve of the crack length *vs*. the CMOD is given in Fig. 20. Some specific crack propagation diagrams are shown in Fig. 21.

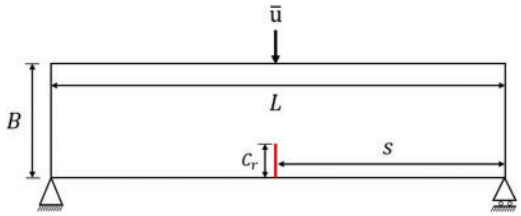

Figure 19: The schematics for the three-point bending test specimen (color online)

Table 7: Calculation parameters for the three-point bending test

E (GPa)	ν	h_r (m)	G_0 (Pa · m)	G_{IC} (Pa · m)	C_r (m)	L (m)	B (m)	s (m)
35.77	0.1	0.015	1.145	9.8	0.045	0.6	0.15	0.3

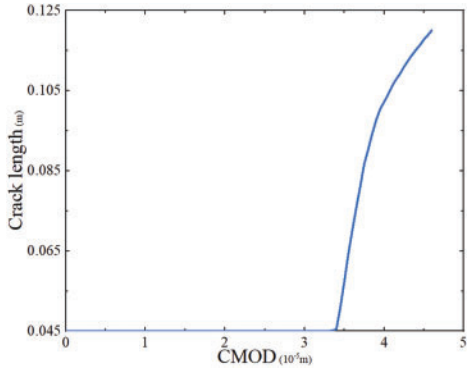

Figure 20: The crack length *vs*. the CMOD (color online)

(a) The CMOD is 33.5μm

(b) The CMOD is 46.0μm

Figure 21: The crack propagation diagram (color online)

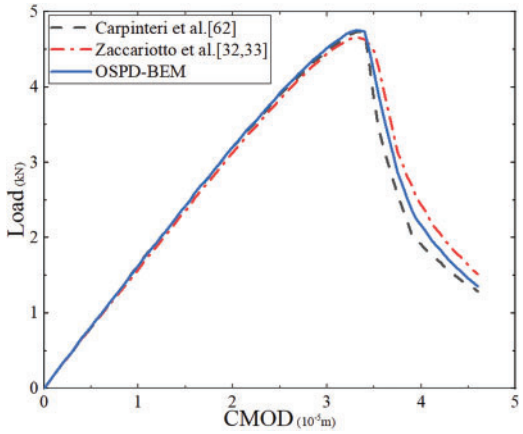

Figure 22: The load *vs*. the CMOD (color online)

The curved line of external load *vs*. CMOD is given in Fig. 22, and we compare OSPD-BEM results with FEM results predicted by Carpinteri et al. [62] and the bond-based peridynamic mesh-free particle method (BBPD-MPM) results predicted by Zaccariotto et al. [32,33] in Fig. 22. We find the result of the OSPD-BEM is closer to those of Carpinteri et al. [62] than those of Zaccariotto et al. [32,33]. The reason stems from the effect of Poisson's ratio. The OSPD-BEM and Carpinteri et al. [62] can adopt a real Poisson's ratio, while Zaccariotto et al. [32,33] is trapped in a fixed Poisson's ratio. As displayed in [65], the effect of Poisson's ratio becomes obvious, when a crack approaches boundary. The crack initiation load F_m (i.e., the peak value in Fig. 22) and its corresponding CMOD U_m in Fig. 22 corresponding to Carpinteri et al. [62], Zaccariotto et al. [32,33] and the OSPD-BEM are shown in Table 8. The prediction of the fracture toughness parameters is close for these three numerical approaches.

Table 8: Fracture toughness comparison

	Carpinteri et al. [62]	Zaccariotto et al. [32,33]	OSPD-BEM
F_m (kN)	4.73	4.66	4.75
U_m (μm)	33.15	33.15	33.15

5 Conclusions

In our research, we propose OSPD-BEM as an enhancement over prior efforts [21]. This method inherits the advantages of the BBPD-BEM [21]. Firstly, it eliminates the boundary softening phenomenon [57] resulting from boundary discretization. Secondly, it facilitates problem-solving in infinite domains. Thirdly, it exhibits advantages in terms of accuracy and efficiency compared to numerical methods that discretize the entire domain. In addition, this method is based on the OSPD, overcoming theoretical limitations present in previous works [21], such as fixed Poisson's ratio. Furthermore, we introduce a fracture calculation model tailored for OSPD-BEM to investigate basic crack propagation problems. In future research, a viable approach to tackling complex crack growth problems, such as multiple cracks and crack branching, might involve the utilization of a coupling

method [66,67]. This method would integrate PD-MPM and OSPD-BEM in a complementary manner, with PD-MPM applied in cracked regions and OSPD-BEM in uncracked regions.

Acknowledgement: We acknowledge the High-Performance Computing Platform of Peking University for providing computational resources.

Funding Statement: The work is supported by the National Key R&D Program of China (2020YFA07 10500).

Author Contributions: The authors confirm contribution to the paper as follows: study conception and design: Xue Liang, Linjuan Wang; data collection: Xue Liang; analysis and interpretation of results: Xue Liang, Linjuan Wang; draft manuscript preparation: Xue Liang, Linjuan Wang. All authors reviewed the results and approved the final version of the manuscript.

Availability of Data and Materials: The data that support the findings of this study are available from the corresponding author upon reasonable request.

Conflicts of Interest: The authors declare that they have no conflicts of interest to report regarding the present study.

References

1. Silling, S. A. (2000). Reformulation of elasticity theory for discontinuities and long-range forces. *Journal of the Mechanics and Physics of Solids, 48(1),* 175–209. https://doi.org/10.1016/S0022-5096(99)00029-0
2. Silling, S. A., Epton, M., Weckner, O., Xu, J., Askari, E. (2007). Peridynamic states and constitutive modeling. *Journal of Elasticity, 88,* 151–184. https://doi.org/10.1007/s10659-007-9125-1
3. Ren, H., Zhuang, X., Rabczuk, T. (2017). Dual-horizon peridynamics: A stable solution to varying horizons. *Computer Methods in Applied Mechanics and Engineering, 318,* 762–782. https://doi.org/10.1016/j.cma.2016.12.031
4. Ren, H., Zhuang, X., Cai, Y., Rabczuk, T. (2016). Dual-horizon peridynamics. *International Journal for Numerical Methods in Engineering, 108(12),* 1451–1476. https://doi.org/10.1002/nme.5257
5. Rabczuk, T., Ren, H., Zhuang, X. (2019). A nonlocal operator method for partial differential equations with application to electromagnetic waveguide problem. *Computers, Materials & Continua, 59(1),* 31–55. https://doi.org/10.32604/cmc.2019.04567
6. Liu, S., Fang, G., Liang, J., Fu, M., Wang, B. (2020). A new type of peridynamics: Element-based peridynamics. *Computer Methods in Applied Mechanics and Engineering, 366,* https://doi.org/10.1016/j.cma.2020.113098
7. Liu, S., Fang, G., Liang, J., Fu, M., Wang, B. et al. (2021). Study of three-dimensional Euler-Bernoulli beam structures using element-based peridynamic model. *European Journal of Mechanics/A Solids, 86,* 104186. https://doi.org/10.1016/j.euromechsol.2020.104186
8. Tian, D., Zhou, X. (2022). A viscoelastic model of geometry-constraint-based non-ordinary state-based peridynamics with progressive damage. *Computational Mechanics, 69,* 1413–1441. https://doi.org/10.1007/s00466-022-02148-z
9. Xiao, Y., Wu, J., Shen, H., Hu, X., Yong, H. (2023). Damage behavior in Bi-2212 round wire with 3D elastoplastic peridynamic. *Acta Mechanica Sinica, 39,* https://doi.org/10.1007/s10409-023-22431-x
10. Liu, D., Liu, N., Zhou, W. (2017). Peridynamic modelling of impact damage in three-point bending beam with offset notch. *Applied Mathematics and Mechanics (English Edition), 38(1),* 99–110. https://doi.org/10.1007/s10483-017-2158-6

11. Wang, X., Tong, Q. (2023). Peridynamic modeling of delayed fracture in electrodes during lithiation. *Computer Methods in Applied Mechanics and Engineering, 404,* 115774. https://doi.org/10.1016/j.cma.2022.115774
12. Ongaro, G., Bertani, R., Galvanetto, U., Pontefisso, A., Zaccariotto, M. (2022). A multiscale peridynamic framework for modelling mechanical properties of polymer-based nanocomposites. *Engineering Fracture Mechanics, 274,* 108751. https://doi.org/10.1016/j.engfracmech.2022.108751
13. Wu, P., Chen, Z. (2023). Peridynamic electromechanical modeling of damaging and cracking in conductive composites: A stochastically homogenized approach. *Composite Structures, 305,* 116528. https://doi.org/10.1016/j.compstruct.2022.116528
14. Silling, S. A., Fermen-Coker, M. (2021). Peridynamic model for microballistic perforation of multilayer graphene. *Theoretical and Applied Fracture Mechanics, 113,* 102947. https://doi.org/10.1016/j.tafmec.2021.102947
15. Nowak, M., Mulewska, K., Azarov, A., Kurpaska, L., Ustrzycka, A. (2023). A peridynamic elasto-plastic damage model for ion-irradiated materials. *International Journal of Mechanical Sciences, 237,* 107806. https://doi.org/10.1016/j.ijmecsci.2022.107806
16. Yang, S., Gu, X., Zhang, Q., Xia, X. (2021). Bond-associated non-ordinary state-based peridynamic model for multiple spalling simulation of concrete. *Acta Mechanica Sinica, 37(7),* 1104–1135. https://doi.org/10.1007/s10409-021-01055-5
17. Silling, S. A., Askari, E. (2005). A meshfree method based on the peridynamic model of solid mechanics. *Theoretical and Applied Fracture Mechanics, 83(17–18),* 1526–1535. https://doi.org/10.1016/j.compstruc.2004.11.026
18. Kilic, B., Madenci, E. (2009). Structural stability and failure analysis using peridynamic theory. *International Journal of Non-Linear Mechanics, 44(8),* 845–854. https://doi.org/10.1016/j.ijnonlinmec.2009.05.007
19. Chen, X., Gunzburger, M. (2011). Continuous and discontinuous finite element methods for a peridynamics model of mechanics. *Computer Methods in Applied Mechanics and Engineering, 200(9–12),* 1237–1250. https://doi.org/10.1016/j.cma.2010.10.014
20. Tian, X., Du, Q. (2013). Analysis and comparison of different approximation to nonlocal diffusion and linear peridynamic equations. *Siam Journal on Numerical Analysis, 51(6),* 3458–3482. https://doi.org/10.1137/13091631X
21. Liang, X., Wang, L., Xu, J., Wang, J. (2021). The boundary element method of peridynamics. *International Journal for Numerical Methods in Engineering, 122(20),* 5558–5593. https://doi.org/10.1002/nme.6764
22. Liu, W., Hong, J. W. (2012). A coupling approach of discretized peridynamics with finite element method. *Computer Methods in Applied Mechanics and Engineering, 245–246,* 163–175. https://doi.org/10.1016/j.cma.2012.07.006
23. Fang, G., Liu, S., Fu, M., Wang, B., Wu, Z. et al. (2019). A method to couple state-based peridynamics and finite element method for crack propagation problem. *Mechanics Research Communications, 95,* 89–95. https://doi.org/10.1016/j.mechrescom.2019.01.005
24. Dong, Y., Su, C., Qiao, P. (2020). A stability-enhanced peridynamic element to couple non-ordinary state-based peridynamics with finite element method for fracture analysis. *Finite Elements in Analysis and Design, 181,* 103480. https://doi.org/10.1016/j.finel.2020.103480
25. Yang, Y., Liu, Y. (2021). Modeling of cracks in two-dimensional elastic bodies by coupling the boundary element method with peridynamics. *International Journal of Solids and Structures, 217–218,* 74–89. https://doi.org/10.1016/j.ijsolstr.2021.02.002
26. Yang, Y., Liu, Y. (2022). Analysis of dynamic crack propagation in two-dimensional elastic bodies by coupling the boundary element method and the bond-based peridynamics. *Computer Methods in Applied Mechanics and Engineering, 399,* 115339. https://doi.org/10.1016/j.cma.2022.115339

27. Kan, X., Zhang, A., Yan, J., Wu, W., Liu, Y. (2020). Numerical investigation of ice breaking by a high-pressure bubble based on a coupled BEM-PD model. *Journal of Fluids and Structures, 96,* 103016. https://doi.org/10.1016/j.jfluidstructs.2020.103016
28. Chen, X., Yu, H. (2022). A multiscale method coupling peridynamic and boundary element models for dynamic problems. *Computer Methods in Applied Mechanics and Engineering, 401,* 115669. https://doi.org/10.1016/j.cma.2022.115669
29. Barenblatt, G. I. (1959). The formation of equilibrium cracks during brittle fracture: General ideas and hypothesis, axially symmetric cracks. *Journal of Applied Mathematics and Mechanics, 23(3),* 622–636. https://doi.org/10.1016/0021-8928(59)90157-1
30. Dugdale, D. S. (1960). Yielding of steel sheets containing slits. *Journal of the Mechanics and Physics of Solids, 8(2),* 100–104. https://doi.org/10.1016/0022-5096(60)90013-2
31. Hillerborg, A., Modeer, M., Petersson, P. E. (1976). Analysis of crack formation and crack growth in concrete by means of fracture mechanics and finite elements. *Cement and Concrete Research, 6(6),* 773–781. https://doi.org/10.1016/0008-8846(76)90007-7
32. Zaccariotto, M., Luongo, F., Sarego, G., Galvanetto, U. (2015). Examples of applications of the peridynamic theory to the solution of static equilibrium problems. *The Aeronautical Journal, 119(1216),* 677–700. https://doi.org/10.1017/S0001924000010770
33. Zaccariotto, M., Mudric, T., Tomasi, D., Shojaei, A., Galvanetto, U. (2018). Coupling of FEM meshes with peridynamic grids. *Computer Methods in Applied Mechanics and Engineering, 330,* 471–497. https://doi.org/10.1016/j.cma.2017.11.011
34. Wang, L., Xu, J., Wang, J. (2019). Elastodynamics of linearized isotropic state-based peridynamic media. *Journal of Elasticity, 137(2),* 157–176. https://doi.org/10.1007/s10659-018-09723-7
35. Wang, L. (2018). *Research on some basic problems of spatiotemporal non-local elasticity (Ph.D. Thesis)*. Peking University, China.
36. Du, Q., Burgunder, M., Lehoucq, R. B., Zhou, K. (2013). A nonlocal vector calculus, nonlocal volume-constrained problems, and nonlocal balance laws. *Mathematical Models and Methods in Applied Sciences, 23(3),* 493–540. https://doi.org/10.1142/S0218202512500546
37. Du, Q., Gunzburger, M., Lehoucq, R. B., Zhou, K. (2013). Analysis of the volume-constrained peridynamic Navier equation of linear elasticity. *Journal of Elasticity, 113(2),* 193–217. https://doi.org/10.1007/s10659-012-9418-x
38. Silling, S. A. (2010). Linearized theory of peridynamic states. *Journal of Elasticity, 99,* 85–111. https://doi.org/10.1007/s10659-009-9234-0
39. Sarego, G., Le, Q. V., Bobaru, F., Zaccariotto, M., Galvanetto, U. (2016). Linearized state-based peridynamics for 2D problems. *International Journal for Numerical Methods in Engineering, 108(10),* 1174–1197. https://doi.org/10.1002/nme.5250
40. Du, Q., Gunzburger, M., Lehoucq, R. B., Zhou, K. (2012). Analysis and approximation of nonlocal diffusion problems with volume constraints. *SIAM Review, 54(4),* 667–696. https://doi.org/10.1137/110833294
41. Mengesha, T., Du, Q. (2014). Nonlocal constrained value problems for a linear peridynamic Navier equation. *Journal of Elasticity, 116,* 27–51. https://doi.org/10.1007/s10659-013-9456-z
42. Seleson, P., Parks, M. L. (2011). On the role of the influence function in the peridynamic theory. *Journal for Multiscale Computational Engineering, 9(6),* 689–706. https://doi.org/10.1615/IntJMultCompEng.2011002527
43. Ren, H., Zhuang, X., Rabczuk, T. (2020). A nonlocal operator method for solving partial differential equations. *Computer Methods in Applied Mechanics and Engineering, 358,* 112621. https://doi.org/10.1016/j.cma.2019.112621
44. Lehoucq, R. B., Silling, S. A. (2008). Force flux and the peridynamic stress tensor. *Journal of the Mechanics and Physics of Solids, 56(4),* 1566–1577. https://doi.org/10.1016/j.jmps.2007.08.004

45. Silling, S. A., Lehoucq, R. B. (2008). Convergence of peridynamics to classical elasticity theory. *Journal of Elasticity, 93,* 13–37. https://doi.org/10.1007/s10659-008-9163-3
46. Aliabadi, M. H. (2002). *The boundary element method*. London: John Wiley and Sons.
47. Scabbia, F., Zaccariotto, M., Galvanetto, U. (2021). A novel and effective way to impose boundary conditions and to mitigate the surface effect in state-based peridynamics. *International Journal for Numerical Methods in Engineering, 122(20),* 5773–5811. https://doi.org/10.1002/nme.6773
48. Scabbia, F., Zaccariotto, M., Galvanetto, U. (2022). A new method based on Taylor expansion and nearest-node strategy to impose Dirichlet and Neumann boundary conditions in ordinary state-based peridynamics. *Computational Mechanics, 70,* 1–27. https://doi.org/10.1007/s00466-022-02153-2
49. Tong, Y., Shen, W., Shao, J., Chen, J. (2020). A new bond model in peridynamics theory for progressive failure in cohesive brittle materials. *Engineering Fracture Mechanics, 223,* 106767. https://doi.org/10.1016/j.engfracmech.2019.106767
50. Tong, Y., Shen, W., Shao, J. (2020). An adaptive coupling method of state-based peridynamics theory and finite element method for modeling progressive failure process in cohesive materials. *Computer Methods in Applied Mechanics and Engineering, 370,* 113248. https://doi.org/10.1016/j.cma.2020.113248
51. Madenci, E., Oterkus, E. (2014). *Peridynamic theory and its applications*. New York: Springer.
52. Zehnder, A. T. (2012). *Fracture mechanics*. London: Springer.
53. Prakash, N., Seidel, G. D. (2015). A novel two-parameter linear elastic constitutive model for bond based peridynamics. *56th AIAA/ASCE/AHS/ASC Structures, Structural Dynamics, and Materials Conference*, Kissimmee, USA.
54. Huang, X., Li, S., Jin, Y., Yang, D., Su, G. et al. (2019). Analysis on the influence of Poisson's ratio on brittle fracture by applying uni-bond dual-parameter peridynamic model. *Engineering Fracture Mechanics, 222,* 106685. https://doi.org/10.1016/j.engfracmech.2019.106685
55. Bruhwiler, E., Wittmann, F. H. (1990). The wedge splitting test, a new method of performing stable fracture mechanics tests. *Engineering Fracture Mechanics, 35(1–3),* 117–125. https://doi.org/10.1016/0013-7944(90)90189-N
56. Trunk, B. (2000). *Einfluss der Bauteilgroesse auf die Bruchenergie von Beton*. German: Aedificatio Publishers.
57. Le, Q. V., Bobaru, F. (2018). Surface corrections for peridynamic models in elasticity and fracture. *Computational Mechanics, 61,* 499–518. https://doi.org/10.1007/s00466-017-1469-1
58. Tian, X., Du, Q., Gunzburger, M. (2016). Asymptotically compatible schemes for the approximation of fractional Laplacian and related nonlocal diffusion problems on bounded domains. *Advances in Computational Mathematics, 42(6),* 1363–1380. https://doi.org/10.1007/s10444-016-9466-z
59. Areias, P. M. A., Belytschko, T. (2005). Analysis of three-dimensional crack initiation and propagation using the extended finite element method. *International Journal for Numerical Methods in Engineering, 63(5),* 760–788. https://doi.org/10.1002/nme.1305
60. Su, X., Yang, Z., Liu, G. (2010). Finite element modelling of complex 3D static and dynamic crack propagation by embedding cohesive elements in abaqus. *Acta Mechanica Solida Sinica, 23(3),* 271–282. https://doi.org/10.1016/S0894-9166(10)60030-4
61. Bie, Y., Cui, X., Li, Z. (2018). A coupling approach of state-based peridynamics with node-based smoothed finite element method. *Computer Methods in Applied Mechanics and Engineering, 331,* 675–700. https://doi.org/10.1016/j.cma.2017.11.022
62. Carpinteri, A., Colombo, G. (1989). Numerical analysis of catastrophic softening behaviour (snap-back instability). *Computers and Structures, 31(4),* 607–636. https://doi.org/10.1016/0045-7949(89)90337-4
63. Dufort, L., Grediac, M., Surrel, Y. (2001). Experimental evidence of the cross-section warping in short composite beams under three point bending. *Composite Structures, 51(1),* 37–47. https://doi.org/10.1016/S0263-8223(00)00121-5

64. Zhang, J., Dong, W., Zhang, B. (2023). Experimental study on local crack propagation of concrete under three-point bending. *Construction and Building Materials, 401,* 132699. https://doi.org/10.1016/j.conbuildmat.2023.132699
65. Sundaram, V. K. A., Madenci, E. (2023). Direct coupling of dual-horizon peridynamics with finite elements for irregular discretization without an overlap zone. *Engineering with Computers, 40,* 605–635. https://doi.org/10.1007/s00366-023-01800-3
66. Han, F., Lubineau, G. (2012). Coupling of nonlocal and local continuum models by the Arlequin approach. *Journal for Numerical Methods in Engineering, 89(6),* 671–685. https://doi.org/10.1002/nme.3255
67. Han, F., Lubineau, G., Azdoud, Y., Askari, A. (2016). A morphing approach to couple state-based peridynamics with classical continuum mechanics. *Computer Methods in Applied Mechanics and Engineering, 301,* 336–358. https://doi.org/10.1016/j.cma.2015.12.024

Appendix A. The Comparison of Different Nonlocal Operators

The literature [36] and the literature [5,43] provide two different nonlocal operators, and both can effectively represent the PD equilibrium equation and boundary condition. The nonlocal gradient, nonlocal curl and nonlocal divergence in both literature is a dual relationship. The nonlocal operators [5,43] is the weighted adjoint operator of the ones [36], if the following conditions are satisfied:

$$\boldsymbol{\beta}\left(\mathbf{x},\mathbf{y}\right)\Gamma\left(\mathbf{x},\mathbf{y}\right)=-\mathbf{r}\cdot\mathbf{K}_{\mathbf{x}}^{-1}w\left(\mathbf{r}\right) \tag{A.1}$$

where the symbol on the left side of Eq. (A.1) appears in Eqs. (6) and (7), and the symbol on the right side of Eq. (A.1) appears in Eq. (6) of the literature [43].

In other words, there are

$$\begin{cases}\mathscr{B}_{\Gamma}^{*}\left(\mathbf{v}_{\mathbf{x}}\right)=\tilde{\nabla}\otimes\mathbf{v}_{\mathbf{x}}\\ \mathscr{T}_{\mathrm{r}}\left(\mathscr{B}_{\Gamma}^{*}\left(\mathbf{v}_{\mathbf{x}}\right)\right)=\tilde{\nabla}\cdot\mathbf{v}_{\mathbf{x}}\end{cases} \tag{A.2}$$

where $\mathscr{B}_{\Gamma}^{*}$ is in Eq. (4), and $\mathscr{T}_{\mathrm{r}}$ denotes the trace operator. The remaining symbols are seen in Eqs. (8) and (14) of the literature [43]. The proof is obvious by the definition. Furthermore, if the adjoint operator of weighted nonlocal curl is defined as follows:

$$\mathscr{C}_{\Gamma}^{*}\left(\mathbf{x}\right)\equiv\int_{\Omega\cup\Omega_{\tau}}\mathscr{C}^{*}\left(\mathbf{P}\right)\left(\mathbf{x},\mathbf{y}\right)\Gamma\left(\mathbf{x},\mathbf{y}\right)\mathrm{d}V_{\mathrm{y}}\qquad\text{for }\mathbf{x}\in\Omega\cup\Omega_{\tau} \tag{A.3}$$

where $\mathbf{P}$ is a vector, $\mathscr{C}^{*}$ is defined as follows:

$$\mathscr{C}^{*}\left(\mathbf{P}\right)\left(\mathbf{x},\mathbf{y}\right)\equiv\boldsymbol{\beta}\left(\mathbf{x},\mathbf{y}\right)\times\left[\mathbf{P}\left(\mathbf{y}\right)-\mathbf{P}\left(\mathbf{x}\right)\right]\qquad\text{for }\mathbf{x},\mathbf{y}\in\Omega\cup\Omega_{\tau} \tag{A.4}$$

The following conditions are satisfied:

$$\boldsymbol{\beta}\left(\mathbf{x},\mathbf{y}\right)\Gamma\left(\mathbf{x},\mathbf{y}\right)=\mathbf{r}\cdot\mathbf{K}_{\mathbf{x}}^{-1}w\left(\mathbf{r}\right) \tag{A.5}$$

Then

$$\mathscr{C}_{\Gamma}^{*}\left(\mathbf{v}_{\mathbf{x}}\right)=\tilde{\nabla}\times\mathbf{v}_{\mathbf{x}} \tag{A.6}$$

where the symbols are seen in Eq. (13) of the literature [43].

Appendix B. The Boundary Integral Equation in the Laplace Domain

It is convenient to deal with the dynamic problem in the Laplace domain for the BEM. It has two prominent advantages, compared with time domain. The first is eliminating time accumulation error; the second is that we can easily implement parallel computation. Thus, we derive the BIE of the OSPD for dynamic problems in Laplace domain as follows. First of all, we give the dynamic equation for the linear elastic OSPD in the Laplace domain

$$\begin{cases} \mathscr{G}\left(\tilde{\mathbf{u}}\right)(\mathbf{x},s)+\tilde{\mathbf{F}}(\mathbf{x},s)=\rho s^2\tilde{\mathbf{u}}(\mathbf{x},s) & \text{for } \mathbf{x}\in\Omega \\ \tilde{\mathbf{u}}(\mathbf{x},s)=\tilde{\mathbf{g}}_d(\mathbf{x},s) & \text{for } \mathbf{x}\in\Omega_{\tau_d} \\ \mathscr{M}\left(\tilde{\mathbf{u}}\right)(\mathbf{x},s)=\tilde{\mathbf{g}}_n(\mathbf{x},s) & \text{for } \mathbf{x}\in\Omega_{\tau_n} \\ \tilde{\mathbf{F}}(\mathbf{x},s)=\tilde{\mathbf{F}}_{\mathrm{b}}(\mathbf{x},s)+\rho s\mathbf{u}(\mathbf{x},t_0)+\rho\dot{\mathbf{u}}(\mathbf{x},t_0) & \\ \mathbf{u}(\mathbf{x},t_0)=\mathbf{u}_0(\mathbf{x}) \qquad \dot{\mathbf{u}}(\mathbf{x},t_0)=\dot{\mathbf{u}}_0(\mathbf{x}) & \end{cases} \tag{B.1}$$

where the operators $\mathscr{G}$ and $\mathscr{M}$ are mentioned in Eq. (11); s is a variable corresponding to the Laplace transformation; ρ is the mass density; $\tilde{\mathbf{u}}$ is the Laplace transformation of the displacement $\mathbf{u}$ in the time domain; $\tilde{\mathbf{g}}_d$ and $\tilde{\mathbf{g}}_n$ are the Laplace transformation of the boundary condition; $\tilde{\mathbf{F}}_{\mathrm{b}}$ is the Laplace transformation of the body force density $\mathbf{F}_{\mathrm{b}}$ in the time domain; t_0 is the initial time; $\mathbf{u}_0$ and $\dot{\mathbf{u}}_0$ are the initial conditions in the time domain.

The weighted residual method is adopted to derive the BIE in Laplace domain instead of the reciprocal theorem, following the derivation in the classical theory. We rewrite Eq. (B.1) in the form of weighted residual as follows:

$$\begin{aligned} &\int_{\Omega_{\tau_n}}\left(\tilde{\mathbf{g}}_n(\mathbf{x},s)-\mathscr{M}\left(\tilde{\mathbf{u}}\right)(\mathbf{x},s)\right)\cdot\tilde{\mathbf{u}}_g(\mathbf{x}-\overline{\mathbf{x}}_m,s)\,\mathrm{d}V_{\mathbf{x}}-\int_{\Omega_{\tau_d}}\left(\tilde{\mathbf{g}}_d(\mathbf{x},s)-\tilde{\mathbf{u}}(\mathbf{x},s)\right)\cdot\mathscr{M}\left(\tilde{\mathbf{u}}_g\right)(\mathbf{x}-\overline{\mathbf{x}}_m,s)\,\mathrm{d}V_{\mathbf{x}} \\ &=\int_{\Omega}\left(-\rho s^2\tilde{\mathbf{u}}(\mathbf{x},s)+\mathscr{G}\left(\tilde{\mathbf{u}}\right)(\mathbf{x},s)+\tilde{\mathbf{F}}(\mathbf{x},s)\right)\cdot\tilde{\mathbf{u}}_g(\mathbf{x}-\overline{\mathbf{x}}_m,s)\,\mathrm{d}V_{\mathbf{x}} \end{aligned} \tag{B.2}$$

where $\tilde{\mathbf{u}}_g(\mathbf{x}-\overline{\mathbf{x}}_m,s)$ is the Green's function in the Laplace domain for the infinite body; it meets the following the equilibrium equation

$$-\mathscr{G}\left(\tilde{\mathbf{u}}_g\right)(\mathbf{x}-\overline{\mathbf{x}}_m,s)+\rho s^2\tilde{\mathbf{u}}_g(\mathbf{x}-\overline{\mathbf{x}}_m,s)=\Xi(\mathbf{x}-\overline{\mathbf{x}}_m)\mathbf{E}_i \tag{B.3}$$

where $\mathbf{E}_i$ is the coordinate base vector; $\Xi(\mathbf{x}-\overline{\mathbf{x}}_m)$ is the Dirac function.

We find that if s is the fixed value, the actual displacement $\tilde{\mathbf{u}}(\mathbf{x},s)$ and the Green's function $\tilde{\mathbf{u}}_g(\mathbf{x}-\overline{\mathbf{x}}_m,s)$ can be regarded as the solutions of a certain static problem. In order to further derive the BIE, we construct two spurious static problems corresponding to $\tilde{\mathbf{u}}(\mathbf{x},s)$ and $\tilde{\mathbf{u}}_g(\mathbf{x}-\overline{\mathbf{x}}_m,s)$, and the static problems must satisfy Eq. (1). Two spurious static states are given as follows:

$$\begin{cases} \mathscr{G}\left(\tilde{\mathbf{u}}\right)(\mathbf{x},s)+\mathbf{F}_{\mathrm{b}}\left(\tilde{\mathbf{u}}\right)(\mathbf{x},s)=\mathbf{0} & \text{for } \mathbf{x}\in\Omega \\ \tilde{\mathbf{u}}(\mathbf{x},s)=\tilde{\mathbf{u}}(\mathbf{x},s) & \text{for } \mathbf{x}\in\Omega_{\tau_d} \\ \mathscr{M}\left(\tilde{\mathbf{u}}\right)(\mathbf{x},s)=\phi\left(\tilde{\mathbf{u}}\right)(\mathbf{x},s) & \text{for } \mathbf{x}\in\Omega_{\tau_n} \end{cases} \tag{B.4}$$

$$\begin{cases} \mathscr{G}\left(\tilde{\mathbf{u}}_g\right)(\mathbf{x}-\overline{\mathbf{x}}_m,s)+\mathbf{F}_{\mathrm{b}}\left(\tilde{\mathbf{u}}_g\right)(\mathbf{x}-\overline{\mathbf{x}}_m,s)=\mathbf{0} & \text{for } \mathbf{x}\in\Omega \\ \tilde{\mathbf{u}}_g(\mathbf{x}-\overline{\mathbf{x}}_m,s)=\tilde{\mathbf{u}}_g(\mathbf{x}-\overline{\mathbf{x}}_m,s) & \text{for } \mathbf{x}\in\Omega_{\tau_d} \\ \mathscr{M}\left(\tilde{\mathbf{u}}_g\right)(\mathbf{x}-\overline{\mathbf{x}}_m,s)=\phi\left(\tilde{\mathbf{u}}_g\right)(\mathbf{x}-\overline{\mathbf{x}}_m,s) & \text{for } \mathbf{x}\in\Omega_{\tau_n} \end{cases} \tag{B.5}$$

where $\mathbf{F}_{\mathrm{b}}\left(\tilde{\mathbf{u}}\right)$ and $\mathbf{F}_{\mathrm{b}}\left(\tilde{\mathbf{u}}_g\right)$ are the body force densities corresponding to $\tilde{\mathbf{u}}$ and $\tilde{\mathbf{u}}_g$, respectively. $\phi\left(\tilde{\mathbf{u}}\right)$ and $\phi\left(\tilde{\mathbf{u}}_g\right)$ are the boundary constraints corresponding to $\tilde{\mathbf{u}}$ and $\tilde{\mathbf{u}}_g$, respectively. These two states satisfy

the reciprocal theorem Eq. (15).

$$\int_{\Omega} \mathscr{G}\left(\tilde{\mathbf{u}}_g\right)\left(\mathbf{x}-\overline{\mathbf{x}}_m, s\right)\cdot\tilde{\mathbf{u}}\left(\mathbf{x}, s\right)-\mathscr{G}\left(\tilde{\mathbf{u}}\right)\left(\mathbf{x}, s\right)\cdot\tilde{\mathbf{u}}_g\left(\mathbf{x}-\overline{\mathbf{x}}_m, s\right) \mathrm{d}V_{\mathbf{x}}$$
$$=\int_{\Omega_\tau} \mathscr{M}\left(\tilde{\mathbf{u}}_g\right)\left(\mathbf{x}-\overline{\mathbf{x}}_m, s\right)\cdot\tilde{\mathbf{u}}\left(\mathbf{x}, s\right)-\mathscr{M}\left(\tilde{\mathbf{u}}\right)\left(\mathbf{x}, s\right)\cdot\tilde{\mathbf{u}}_g\left(\mathbf{x}-\overline{\mathbf{x}}_m, s\right) \mathrm{d}V_{\mathbf{x}} \tag{B.6}$$

Substituting Eq. (B.6) into Eq. (B.2), we obtain

$$\int_{\Omega}\left(\mathscr{G}\left(\tilde{\mathbf{u}}_g\right)\left(\mathbf{x}-\overline{\mathbf{x}}_m, s\right)-\rho s^2\tilde{\mathbf{u}}_g\left(\mathbf{x}-\overline{\mathbf{x}}_m, s\right)\right)\cdot\tilde{\mathbf{u}}\left(\mathbf{x}, s\right) \mathrm{d}V_{\mathbf{x}}+\int_{\Omega}\tilde{\mathbf{F}}\left(\mathbf{x}, s\right)\cdot\tilde{\mathbf{u}}_g\left(\mathbf{x}-\overline{\mathbf{x}}_m, s\right) \mathrm{d}V_{\mathbf{x}}$$
$$=\int_{\Omega_{\tau_n}}\left(\tilde{\mathbf{g}}_n\left(\mathbf{x}, s\right)-\mathscr{M}\left(\tilde{\mathbf{u}}\right)\left(\mathbf{x}, s\right)\right)\cdot\tilde{\mathbf{u}}_g\left(\mathbf{x}-\overline{\mathbf{x}}_m, s\right) \mathrm{d}V_{\mathbf{x}}-\int_{\Omega_{\tau_d}}\left(\tilde{\mathbf{g}}_d\left(\mathbf{x}, s\right)-\tilde{\mathbf{u}}\left(\mathbf{x}, s\right)\right)\cdot\mathscr{M}\left(\tilde{\mathbf{u}}_g\right)\left(\mathbf{x}-\overline{\mathbf{x}}_m, s\right) \mathrm{d}V_{\mathbf{x}}$$
$$+\int_{\Omega_\tau} \mathscr{M}\left(\tilde{\mathbf{u}}_g\right)\left(\mathbf{x}-\overline{\mathbf{x}}_m, s\right)\cdot\tilde{\mathbf{u}}\left(\mathbf{x}, s\right)-\mathscr{M}\left(\tilde{\mathbf{u}}\right)\left(\mathbf{x}, s\right)\cdot\tilde{\mathbf{u}}_g\left(\mathbf{x}-\overline{\mathbf{x}}_m, s\right) \mathrm{d}V_{\mathbf{x}} \tag{B.7}$$

Substituting Eqs. (B.1) and (B.3) into Eq. (B.7) and dividing the integral domain Ω_τ in the third integral on the right hand side of Eq. (B.7) into two parts Ω_{τ_d} and Ω_{τ_n}, we get

$$\int_{\Omega}\Xi\left(\mathbf{x}-\overline{\mathbf{x}}_m\right)\mathbf{E}_i\cdot\tilde{\mathbf{u}}\left(\mathbf{x}, s\right) \mathrm{d}V_{\mathbf{x}}-\int_{\Omega}\tilde{\mathbf{F}}\left(\mathbf{x}, s\right)\cdot\tilde{\mathbf{u}}_g\left(\mathbf{x}-\overline{\mathbf{x}}_m, s\right) \mathrm{d}V_{\mathbf{x}}$$
$$=\int_{\Omega_{\tau_d}} \mathscr{M}\left(\tilde{\mathbf{u}}\right)\left(\mathbf{x}, s\right)\cdot\tilde{\mathbf{u}}_g\left(\mathbf{x}-\overline{\mathbf{x}}_m, s\right)-\mathscr{M}\left(\tilde{\mathbf{u}}_g\right)\left(\mathbf{x}-\overline{\mathbf{x}}_m, s\right)\cdot\tilde{\mathbf{u}}\left(\mathbf{x}, s\right) \mathrm{d}V_{\mathbf{x}}$$
$$+\int_{\Omega_{\tau_n}} \mathscr{M}\left(\tilde{\mathbf{u}}\right)\left(\mathbf{x}, s\right)\cdot\tilde{\mathbf{u}}_g\left(\mathbf{x}-\overline{\mathbf{x}}_m, s\right)-\mathscr{M}\left(\tilde{\mathbf{u}}_g\right)\left(\mathbf{x}-\overline{\mathbf{x}}_m, s\right)\cdot\tilde{\mathbf{u}}\left(\mathbf{x}, s\right) \mathrm{d}V_{\mathbf{x}} \tag{B.8}$$

Considering the extra condition Eq. (16), which converts the integral in the volume constrained boundary to the one on the classical boundary, we simplify Eq. (B.8) as follows:

$$\int_{\Omega}\Xi\left(\mathbf{x}-\overline{\mathbf{x}}_m\right)\mathbf{E}_i\cdot\tilde{\mathbf{u}}\left(\mathbf{x}, s\right) \mathrm{d}V_{\mathbf{x}}-\int_{\Omega}\tilde{\mathbf{F}}\left(\mathbf{x}, s\right)\cdot\tilde{\mathbf{u}}_g\left(\mathbf{x}-\overline{\mathbf{x}}_m, s\right) \mathrm{d}V_{\mathbf{x}}$$
$$=\int_{\partial\Omega_d}\overline{\mathbf{T}}\left(\tilde{\mathbf{u}}\right)\left(\mathbf{x}, \mathbf{n}, s\right)\cdot\tilde{\mathbf{u}}_g\left(\mathbf{x}-\overline{\mathbf{x}}_m, s\right)-\overline{\mathbf{T}}\left(\tilde{\mathbf{u}}_g\right)\left(\mathbf{x}-\overline{\mathbf{x}}_m, \mathbf{n}, s\right)\cdot\tilde{\mathbf{u}}\left(\mathbf{x}, s\right) \mathrm{d}V_{\mathbf{x}}$$
$$+\int_{\partial\Omega_n}\overline{\mathbf{T}}\left(\tilde{\mathbf{u}}\right)\left(\mathbf{x}, \mathbf{n}, s\right)\cdot\tilde{\mathbf{u}}_g\left(\mathbf{x}-\overline{\mathbf{x}}_m, s\right)-\overline{\mathbf{T}}\left(\tilde{\mathbf{u}}_g\right)\left(\mathbf{x}-\overline{\mathbf{x}}_m, \mathbf{n}, s\right)\cdot\tilde{\mathbf{u}}\left(\mathbf{x}, s\right) \mathrm{d}V_{\mathbf{x}} \tag{B.9}$$

where $\overline{\mathbf{T}}$ is the PD force flux vector operator in Eq. (18) [44,45]. Taking the limit process $\overline{\mathbf{x}}_m \to \partial\Omega_d \cup \partial\Omega_n$ for Eq. (B.9), which is similar to Eq. (28), and executing the variable substitution $\mathbf{x} \to \mathbf{y}, \overline{\mathbf{x}}_m \to \mathbf{x}$,

we get as follows:

$$\begin{aligned}
&\tilde{\mathbf{u}}_k(\mathbf{x},s)-\int_{\Omega}\tilde{\mathbf{F}}(\mathbf{y},s)\cdot\tilde{\mathbf{u}}_g(\mathbf{y}-\mathbf{x},s)\,\mathrm{d}V_{\mathbf{y}}\\
&=\int_{\partial\Omega_d}\overline{\mathbf{T}}\left(\tilde{\mathbf{u}}\right)(\mathbf{y},\mathbf{n},s)\cdot\tilde{\mathbf{u}}_g(\mathbf{y}-\mathbf{x},s)-\overline{\mathbf{T}}\left(\tilde{\mathbf{u}}_g\right)(\mathbf{y}-\mathbf{x},\mathbf{n},s)\cdot\tilde{\mathbf{u}}(\mathbf{y},s)\,\mathrm{d}V_{\mathbf{y}}\\
&\quad+\int_{\partial\Omega_n}\overline{\mathbf{T}}\left(\tilde{\mathbf{u}}\right)(\mathbf{y},\mathbf{n},s)\cdot\tilde{\mathbf{u}}_g(\mathbf{y}-\mathbf{x},s)-\overline{\mathbf{T}}\left(\tilde{\mathbf{u}}_g\right)(\mathbf{y}-\mathbf{x},\mathbf{n},s)\cdot\tilde{\mathbf{u}}(\mathbf{y},s)\,\mathrm{d}V_{\mathbf{y}}
\end{aligned}\tag{B.10}$$

where $\int$ denotes the CPV of the integral. Adopting the approach in the literature [47,48] to establish a connection between the PD boundary conditions and the local boundary conditions, we obtain the following relationship.

$$\tilde{\mathbf{u}}(\mathbf{x},s)=\mathbf{D}(\mathbf{x},s)\quad\text{for }\mathbf{x}\in\partial\Omega_d\tag{B.11}$$

$$\overline{\mathbf{T}}\left(\tilde{\mathbf{u}}\right)(\mathbf{x},\mathbf{n},s)=\mathbf{P}(\mathbf{x},s)\quad\text{for }\mathbf{x}\in\partial\Omega_n\tag{B.12}$$

where $\mathbf{D}(\mathbf{x},s)$ and $\mathbf{P}(\mathbf{x},s)$ are the local boundary condition in the Laplace domain. Substituting Eqs. (B.11) and (B.12) into Eq. (B.10) yields

$$\begin{aligned}
&\tilde{\mathbf{u}}_k(\mathbf{x},s)-\int_{\Omega}\tilde{\mathbf{F}}(\mathbf{y},s)\cdot\tilde{\mathbf{u}}_g(\mathbf{y}-\mathbf{x},s)\,\mathrm{d}V_{\mathbf{y}}\\
&=\int_{\partial\Omega_d}\overline{\mathbf{T}}\left(\tilde{\mathbf{u}}\right)(\mathbf{y},\mathbf{n},s)\cdot\tilde{\mathbf{u}}_g(\mathbf{y}-\mathbf{x},s)-\overline{\mathbf{T}}\left(\tilde{\mathbf{u}}_g\right)(\mathbf{y}-\mathbf{x},\mathbf{n},s)\cdot\mathbf{D}(\mathbf{y},s)\,\mathrm{d}V_{\mathbf{y}}\\
&\quad+\int_{\partial\Omega_n}\mathbf{P}(\mathbf{y},s)\cdot\tilde{\mathbf{u}}_g(\mathbf{y}-\mathbf{x},s)-\overline{\mathbf{T}}\left(\tilde{\mathbf{u}}_g\right)(\mathbf{y}-\mathbf{x},\mathbf{n},s)\cdot\tilde{\mathbf{u}}(\mathbf{y},s)\,\mathrm{d}V_{\mathbf{y}}
\end{aligned}\tag{B.13}$$

Eq. (B.13) is the BIE of the OSPD in the Laplace domain.